Journal of Petrology

Journal of Petrology, 2021, Vol. 62, No. 12, 1–26
https://doi.org/10.1093/petrology/egab097
Advance Access Publication Date: 2 December 2021
Original Manuscript

OXFORD

Melt- to Shear-Controlled Exhumation of Granulites in Granite–Gneiss Domes: Petrological Perspectives from Metapelite of the Neoarchean Ha-Tshanzi Structure, Central Zone, Limpopo Complex, South Africa

Oleg G. Safonov[1,2,3,*], Vasily O. Yapaskurt[2], Marlina A. Elburg[2], Dirk D. van Reenen[3], H. M. Rajesh[4], C. Andre Smit[3], Alexei L. Perchuk[1,2], and Valentina G. Butvina[1]

[1]Korzhinskii Institute of Experimental Mineralogy, Russian Academy of Sciences, Academician Ossipyan str., 4, Chernogolovka, Moscow district, 142432 Russia; [2]Department of Petrology and Volcanology, Geological Faculty, Lomonosov Moscow State University, Moscow, Russia; [3]Department of Geology, University of Johannesburg, Johannesburg, South Africa; and [4]Department of Earth and Environmental Sciences, BIUST, Botswana

*Corresponding author. Telephone and fax: +7-496-525-44-25. E-mail: oleg@iem.ac.ru

Received 29 January 2021; Revised 26 November 2021; Accepted 29 November 2021

Abstract

Gneiss domes cored by migmatites and granites represent the principal role of anatectic melts during the exhumation of high-grade metamorphic complexes. This study explores the exhumation history of a metapelitic granulite within the Ha-Tshanzi structure from the Central Zone of the Neoarchean–Paleoproterozoic Limpopo high-grade Complex, South Africa. Quartzofeldspathic garnet-bearing coarse-grained leucosomes in the rock alternate with attenuated shear bands consisting of biotite, cordierite, sillimanite and quartz that prominently modified the earlier garnet porphyroblasts. Cores of garnet porphyroblasts contain various polyphase inclusions that are interpreted as crystallized inclusions of melt. The phase equilibria modeling and regular zoning of garnet with respect to major (Mg, Fe, Ca) and some trace (P, Cr, Sc) elements reveals that a garnet + biotite + plagioclase + quartz ± sillimanite assemblage in the rock coexisted with the melt during the sub-isothermal (810–830 °C) exhumation from pressure of 10·0–10·2 kbar to 7·5–7·0 kbar during the Neoarchean event (2·68–2·62 Ga). The exhumation mediated by anatectic melt supports interpretation of the Ha-Tshanzi structure as a diapir-related granite–gneiss dome. During upwelling of the dome, the melt segregated into leucosome, while growth of cordierite sequestered water from the melt, assisting its crystallization at the end of the sub-isothermal decompression stage. As the rheology of the rock changed, melt-dominated deformation was transformed to solid-dominated ductile shear deformation. In contrast to the earlier sub-isothermal decompression *P*–*T* path, the gentler slope of ~75 °C $kbar^{-1}$ of the decompression-cooling path marks the exhumation from pressures of ~7 kbar to pressures of 5–4·5 kbar and cooling to 600–550 °C. Dating of zircon, monazite and rutile shows that the Neoarchean evolution of the metapelite was strongly overprinted by the Paleoproterozoic event at *c*. 2·01 Ga. The results of the study highlight the significance of domed structures related to granitic diapirs in the exhumation of the Central Zone of the Limpopo Complex.

Key words: Limpopo Complex; exhumation; metapelite; partial melting; P–T path; shearing deformation

INTRODUCTION

Gneiss domes cored by migmatites and granites are common structures in orogens from the Archean to Cenozoic (e.g. Brun *et al*., 1981; Brown & Dallmeyer, 1996; Vanderhaeghe & Teyssier, 2001; Teyssier & Whitney, 2002; Whitney *et al*., 2004; Yin, 2004; Vanderhaeghe, 2009; Kruckenberg *et al*., 2011; Wiest *et al*., 2020; and references in these papers). Since the pioneering petrological study by Eskola (1948) and later theoretical models (e.g. Ramberg, 1981), granitic diapirism (gravitational upwelling) was favored as a model for gneiss dome genesis, although models related to crustal shortening (folding) and extension (core complex formation) are also popular (see reviews by Teyssier & Whitney, 2002; Whitney *et al*., 2004; Yin, 2004). In addition to specific structural features indicating nearly vertical flow of the crustal material (e.g. Yin, 2004), gneiss domes related to diapirism show the following fundamental petrological features, which distinguish them from other dome-forming mechanisms (e.g. Teyssier & Whitney, 2002; Whitney *et al*., 2004). Rocks from cores of gneiss domes commonly record elevated pressure, which may even be the highest pressures preserved within a given metamorphic terrane. A *P*–*T* path indicative of sub-isothermal decompression (± slight heating) is common for cores of gneiss domes, with the typical magnitude of pressure drop in the migmatitic cores of domes being at least 4–6 kbar (e.g. Teyssier & Whitney, 2002; Whitney *et al*., 2004). Diatexites and granitoids in cores of the domes manifest the leading role of anatectic melts in the development of the diapiric domed structures. There is a close interplay between sub-isothermal decompression, which commonly induces partial melting (e.g. Vielzeuf & Holloway, 1988; Weinberg & Hasalová, 2015), the formation of melt-weakened migmatitic crust with reduced viscosity and, thus, buoyancy-driven exhumation within domes (e.g. Weinberg & Podladchikov, 1995; Weinberg, 1997; Jamieson *et al*., 2011; Lexa *et al*., 2011). The sub-isothermal decompression stage of the exhumation within the granite–gneiss domes is usually followed by gentler decompression cooling or sub-isobaric cooling paths, which reflect a relatively rapid decrease of temperature during decompression in the regime of extensional tectonics (Brown & Dallmeyer, 1996; Teyssier & Whitney, 2002; Whitney *et al*., 2004).

In deeply eroded Archean high-grade terranes, the gneiss domes are usually expressed as oval-shaped structures, which structurally are very similar to regional-scale cylindrical sheath folds (e.g. Roering *et al*., 1992; Dirks *et al*., 1997; Gervais *et al*., 2004; Boshoff *et al*., 2006; Perchuk *et al*., 2008*a*, 2008*b*; Smit *et al*., 2011). In this case, the above-mentioned petrological characteristics can be taken as necessary but not sufficient data to distinguish domes related to granitic diapirism from structures formed by folding and/or shearing. The kilometer-scale rounded structures that occur throughout the Central Zone of the Neoarchean–Paleoproterozoic Limpopo Complex in South Africa (Fig. 1a) are illustrative examples of such structures in high-grade terranes (Roering *et al*., 1992; Perchuk *et al*., 2008*a*, 2008*b*; Smit *et al*., 2011; van Reenen *et al*., 2019). These inclined cylindrical structures were initially interpreted either as large sheath folds associated with NE-directed shear deformation (e.g. Roering *et al*., 1992) or as results of superimposed folding (Watkeys, 1979; Fripp, 1983; Holzer *et al*., 1998) during exhumation of the Central Zone. In view of their ambiguous structural setting, the non-genetic structural term ‘closed structure’ was introduced by South African geologists (S. McCourt, personal communication; Roering *et al*., 1992; Smit *et al*., 2011). The fact that these structures are either cored by granitoids or associated with leucocratic granitoids and/or migmatites became the preposition to relate formation of closed structures to granitic diapirism during the Neoarchean exhumation of the Central Zone (e.g. Perchuk *et al*., 2008*a*, 2008*b*; Smit *et al*., 2011; van Reenen *et al*., 2019). Using local mineral equilibria, Perchuk *et al*. (2008*a*) approximated the evolution of these structures by a decompression-cooling *P*–*T* path from 850–900 °C/8·0–8·5 kbar to 550–600 °C/4·5–5·0 kbar, which implies exhumation in the middle crust. However, the d*P*/d*T* slope of ~75 °C $kbar^{-1}$ of this path and the short depth interval (3–4 kbar) of exhumation contradict the sub-isothermal *P*–*T* evolution that would be expected for rapid diapiric exhumation of material from the lower crust within gneiss domes (e.g. Teyssier & Whitney, 2002; Whitney *et al*., 2004).

The present paper describes the results of a petrological modeling of *P*–*T* evolution of a representative sample of metapelitic granulite from the Ha-Tshanzi closed structure, which is one of the largest in the Central Zone (CZ) of the Limpopo Complex, South Africa (Fig. 1a and b). The goal of the study is to re-evaluate peak *P*–*T* conditions and a *P*–*T* path for the evolution of this rock to demonstrate the principal role of anatectic melts in the post-peak exhumation of metapelites from the closed structure, thereby assessing its interpretation as a diapir-related granite–gneiss dome.

GEOLOGICAL SETTING

General geology and metamorphic evolution of the Central Zone of the Limpopo Complex

The Central Zone (CZ) forms the core of the Limpopo Complex, the Neoarchean–Paleoproterozoic (2·72–2·01 Ga) high-grade gneiss terrane that was exhumed between the Kaapvaal and Zimbabwe cratons (Fig. 1a–c; van Reenen *et al*., 2019, and references therein). The dominant lithological unit of the CZ is the >3·57 Ga Beit Bridge Complex (e.g. Kröner *et al*., 2018), which comprises supracrustal quartzites, magnetite-bearing quartzites, marbles and calc-silicate gneisses, amphibolites, garnet–biotite paragneisses and quartzofeldspathic orthogneisses, as well as less abundant metapelites (Fig. 1c). Precursors of the layered mafic and ultramafic rocks of the Messina Suite and the migmatitic Sand River tonalite–trondhjemite–granodiorite orthogneisses intruded metasedimentary rocks of the Beit Bridge Complex at 3·34–3·33 Ga and 3·31–3·27 Ga, respectively (Fig. 1c; e.g. Kröner *et al*., 2018).

The >3·0 Ga rock association was intruded by precursors of various Neoarchean orthogneisses: the 2·65–2·62 Ga biotite ± garnet ± amphibole-bearing Verbaard and Alldays granitoids (Kröner *et al*., 1999, 2018; Zeh *et al*., 2007; Rajesh *et al*., 2018*b*), the 2·65–2·63 Ga Avoca granitoids (Boshoff *et al*., 2006; van Reenen *et al*., 2008), and the 2·68–2·62 Ga Singelele leucogranites (Kröner *et al*., 1999, 2018; Zeh *et al*., 2007; van Reenen *et al*., 2008; Rajesh *et al*., 2018*a*). The Singelele event represents a leucogranite episode and is considered to be a product of extensive anatexis in the CZ (Fig. 1c; e.g. Rajesh *et al*., 2018*a*, and references therein). An important time marker for the Neoarchean evolution of the CZ is the mainly undeformed porphyritic pyroxene-bearing and pyroxene-free Bulai granitoids (Laurent *et al*., 2011, 2013) that intruded the CZ in the period 2·61–2·58 Ga at the end of the Neoarchean tectonothermal event (Fig. 1a–c).

The CZ shows evidence for a complex succession of superimposed high-grade fold and shear deformational events that predate and postdate emplacement of the Bulai pluton (Fig. 1b and c) (e.g. Roering *et al*., 1992; Boshoff *et al*., 2006; van Reenen *et al*., 2008, 2019; Smit *et al*., 2011). The earliest regional deformational event at 2·72–2·65 Ga is recognized as steeply dipping isoclinal folds

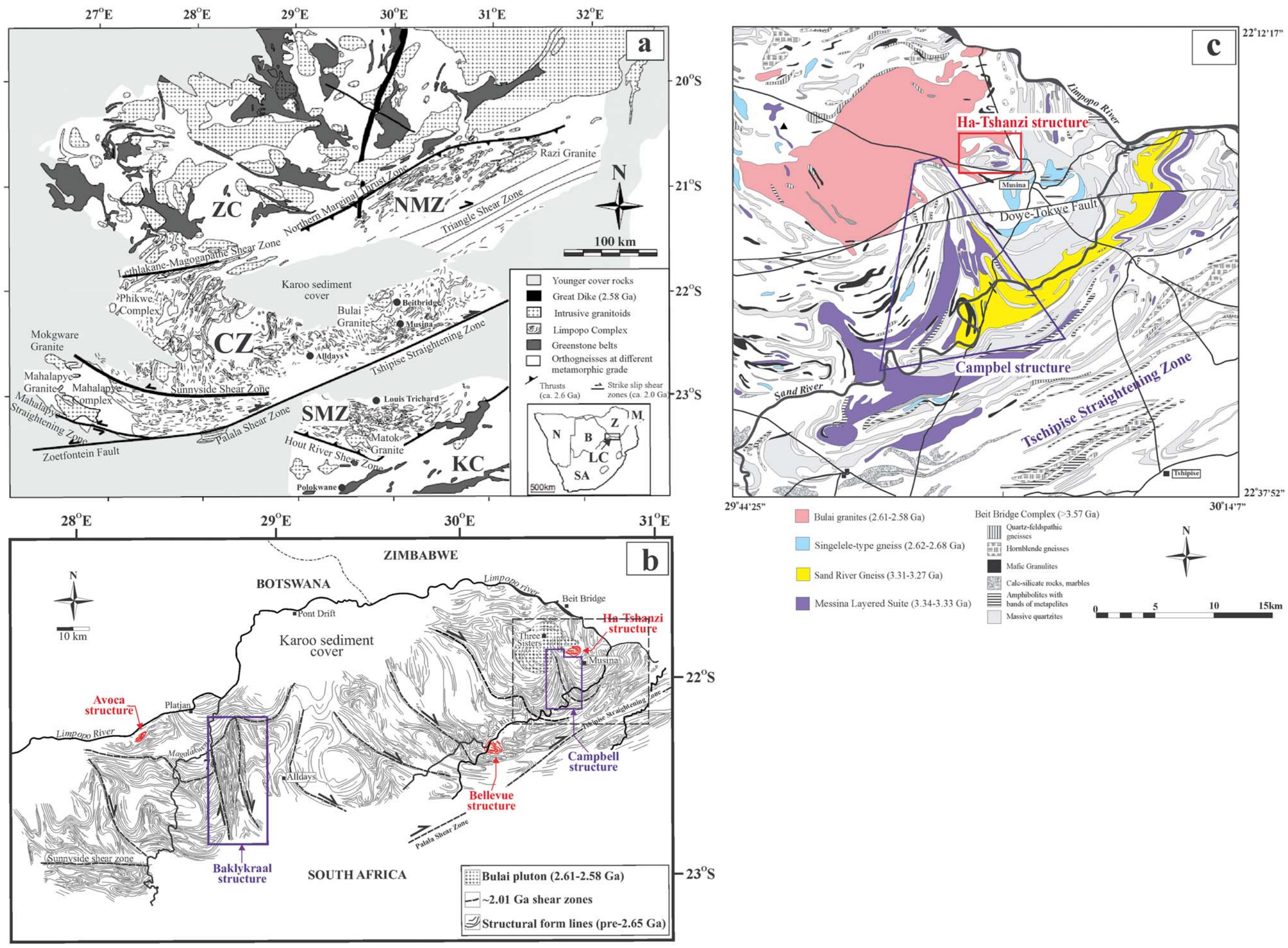

Fig. 1. Geological setting and structure of the Central Zone of the Limpopo high-grade complex. (a) Regional geological map of the Limpopo high-grade complex (Smit *et al*., 2011; van Reenen *et al*., 2019) and the adjacent Kaapvaal (KC) and Zimbabwe (ZC) cratons. The Limpopo Complex is subdivided into three tectonic zones: the Southern Marginal Zone (SMZ), Central Zone (CZ) and Northern Marginal Zone (NMZ). Neoarchaean inward-dipping thrusts separate the granulite-facies terrane of the Limpopo Complex from the adjacent low-grade cratons. The Central Zone forms a core of the complex and is bounded in the south and the north by Neoarchaean dip-slip shear zones (Triangle SZ in the north and Tshipise Straightening Zone in the south), that were reactivated as strike-slip shear zones in the Palaeoproterozoic. The inset shows the geographical position of the Limpopo Complex (LC) at the borders of South Africa (SA), Zimbabwe (Z) and Botswana (B) (N, Namibia; M, Mozambique). (b) Photogeological interpretation of major fold and shear deformational features of the Central Zone (Smit *et al*., 2011; van Reenen *et al*., 2019). Structural form lines (thin black lines) highlight large migmatitic domes and regional-scale isoclinal folds that collectively reflect the earliest (pre-2·65 Ga) deformational features of the CZ. They are overprinted by large north–south-trending fold structures referred to as 'cross folds' (Baklykraal, Campbell) (marked by blue frames) and by large closed structures initially mapped as sheath folds (Avoca, Ha-Tshanzi, Bellevue) (structural lines are highlighted in red). The presence of a numerous closed structures developed near the Bellevue structure should be noted. Thick dashed north–south-trending lines are discrete *c*. 2·0 Ga shear zones (half-headed arrows indicate their kinematics). The SW–NE-trending and steeply SW-dipping Tshipise Straightening Zone bounds the CZ in the south. The 2·61–2·58 Ga Bulai granitic pluton is post-tectonic. Dashed frame indicates the position of the map in (c) (Mussina area). (c) Principal geological units, lithologies and structures of the CZ exposed within the Mussina area [see (b)] (after Smit *et al*., 2011). The Ha-Tshanzi structure is marked with a red frame.

with near-vertical foliation (Fig. 1b). These structures are associated with intensely deformed lithologies that preserve evidence for static recrystallization/recovery at high-temperature conditions reflected by granoblastic textures of rocks. Shear deformational features superimposed onto early isoclinal regional folds collectively reflect the NE-directed exhumation of granulites prior to emplacement of the Bulai pluton (e.g. Smit *et al*., 2011; van Reenen *et al*., 2019). They comprise the >20 km wide ENE–WSW-trending Tshipise Straightening Zone, a deep crustal steeply SW-dipping shear zone bounding the CZ in the south (Fig. 1b) (Horrocks, 1983; Holzer *et al*., 1998), the north–south-trending Campbell and Baklykraal structures referred to as 'cross folds' (Fig. 1b and c), and regional rounded structures termed 'closed structures' (Roering *et al*., 1992; van Kal, 2004; Smit *et al*., 2011) (the Ha-Tshanzi, Bellevue and Avoca structures in Fig. 1b and c are examples). Shear deformational features are characterized by penetrative stretching mineral lineations that are often accompanied by winged porphyroblasts that record exhumation of granulites towards the NE (Roering *et al*., 1992; Holzer *et al*., 1998; van Kal, 2004; Boshoff *et al*., 2006; Smit *et al*., 2011; van Reenen *et al*., 2019).

The Archean rocks are variably overprinted by the Paleoproterozoic event at *c*. 2·01 Ga that was not associated with major fold deformation (Jaeckel *et al*., 1997; Kröner *et al*., 1998, 2018; van Reenen *et al*., 2008, 2019; Smit *et al*., 2011). Shear deformation associated with this event is manifested by discrete centimeter to meters wide north–south-trending shear zones that overprint the main shear fabric of the Tshipise Straightening Zone, the Campbell and Baklykraal 'cross-fold' structures, and the contact of the Bulai Pluton with Ha-Tshanzi (Fig. 1b and c; Holzer *et al*., 1998; Smit *et al*., 2011). Formation of these structures accompanied a regional thermal overprint (Boshoff *et al*., 2006; van Reenen *et al*., 2008, 2019; Perchuk *et al*., 2008*a*, 2008*b*; Smit *et al*., 2011), which was, probably, associated with the influence of the Bushveld large igneous province (LIP) magmatism at *c*. 2·05 Ga (e.g. Millonig *et al*., 2010; Smit *et al*., 2011; Rajesh *et al*., 2020). The Paleoproterozoic magmatic activity is mainly expressed as minor *c*. 2·01 Ga anatectic intrusions and late granite pegmatites in the eastern and central areas of the CZ (e.g. Jaeckel *et al*., 1997; Kröner *et al*., 1998, 1999; van Reenen *et al*., 2008). In contrast, the western areas of the CZ show larger magmatic bodies including the Mahalapye Complex in Botswana (e.g. Hisada *et al*., 2005; Zeh *et al*., 2007; Millonig *et al*., 2010; Rajesh *et al*., 2020; Fig. 1a). Such variable distribution of the products of the *c*. 2·01 Ga Paleoproterozoic magmatic activity is explained by difference in the erosional level that is exposed in the eastern (deeper level) and the western (shallower level) domains of the CZ (e.g. Smit *et al*., 2011).

Thus, available structural data from the CZ indicate the prominence of three high-grade tectono-metamorphic events at 2·72–2·66, 2·65–2·62, and *c*. 2·02 Ga (Jaeckel *et al*., 1997; Holzer *et al*., 1998; Kröner *et al*., 1999, 2018; Zeh *et al*., 2004, 2007; Boshoff *et al*., 2006; Perchuk *et al*., 2008*a*, 2008*b*; van Reenen *et al*., 2008, 2019; Kramers & Mouri, 2011; Smit *et al*., 2011; Brandt *et al*., 2018). However, the discrimination between these events is highly controversial (e.g. Kramers & Mouri, 2011; Kröner *et al*., 2018). Geochronological records on the Neoarchean metamorphic event are rarely preserved in rocks outside the Bulai pluton (Kröner *et al*., 1998; Boshoff *et al*., 2006; van Reenen *et al*., 2008). However, Kröner *et al*. (2018) recently derived U–Pb zircon sensitive high-resolution ion microprobe (SHRIMP) metamorphic ages of 2·65–2·62 Ga from the Beit Bridge Complex rocks occurring as 'xenoliths' within the Bulai pluton (see also Millonig *et al*., 2008). In contrast, evidence for the Paleoproterozoic event (*c*. 2·02 Ga) is abundantly recorded in metamorphic zircon, monazite and rutile in metapelites outside the Bulai pluton (e.g. Kröner *et al*., 2018).

The controversy regarding the specifics of high-grade metamorphic events that affected the CZ in the Neoarchean and Paleoptroterozoic is expressed by different interpretations on its metamorphic evolution. Millonig *et al*. (2008), who studied granulites in xenoliths within the Bulai pluton, concluded that the CZ experienced a single-phase high-grade metamorphism at *c*. 2·6 Ga. On the other hand, Holzer *et al*. (1998), Kröner *et al*. (1999), Schäller *et al*. (1999) and Zeh *et al*. (2004, 2007) rejected evidence for the Neoarchean high-grade event and instead argued that the complex deformational pattern of the CZ (Fig. 1b and c) is the result of a single Palaeoproterozoic tectono-metamorphic event. Perchuk *et al*. (2008*b*), van Reenen *et al*. (2008, 2019) and Smit *et al*. (2011) proposed a composite *P–T–t* path for the polymetamorphic evolution of the CZ that is expressed in distinct Neoarchean and Paleoproterozoic segments. These researchers deduced a two-stage decompression-cooling *P–T* path from 850–900 °C/8·5 kbar to 700 °C/6·0 kbar and from 700 °C/6 bar 550 °C/4·5 kbar reflecting the Neoarchean exhumation of the entire CZ prior to emplacement of the Bulai pluton. The *P–T* path for the final exhumation of the CZ to depths of 9–10 km during the Paleoproterozoic event was constructed from rocks sampled from *c*. 2·01 Ga shear zones superimposed onto the main shear fabric of the Campbell and Baklykraal cross-folds (Fig. 1b and c; Boshoff *et al*., 2006; van Reenen *et al*., 2008; Smit *et al*., 2011). Perchuk *et al*. (2008*b*) proposed that the Neoarchean and Paleoproterozoic *P–T* paths were connected by a stage of sub-isobaric heating at 4·5–5·0 kbar to 650–700 °C. Brandt *et al*. (2018) and Kröner *et al*. (2018) supported the polymetamorphic evolution of the CZ, but interpreted these two events as the result of Neoarchean (2·65–2·62 Ga) continent–continent collision expressed by a counterclockwise *P–T* path that was followed at *c*. 2·01 Ga by a Paleoproterozoic transpressive event linked to a clockwise *P–T* path.

The Ha-Tshanzi closed structure and location of the studied metapelitic granulite

Regional large-scale oval-shaped ('closed', Roering *et al*., 1992) structures are randomly distributed throughout the CZ (Figs 1b, c and 2a) and developed in different rock types. Stereographic projections comprising poles to foliation planes and linear elements from each of these structures [Fig. a, b and c; Supplementary Materials Fig. S1. (supplementary data are available for downloading at http://www.petrology.oxfordjournals.org); see also Roering *et al*., 1992; van Kal, 2004; Boshoff *et al*., 2006; van Reenen *et al*., 2008, 2019; Smit *et al*., 2011] indicate that the closed structures are inclined cylindrical bodies plunging parallel to each other at similar angles of 40–45° towards the SW. These structural features reflect an exhumation of the entire CZ at *c*. 2·6 Ga.

The Ha-Tshanzi closed structure located 6 km NW of Mussina (Fig. 1b) has nearly ellipsoid shape (4 km long, 3 km wide with long axis oriented east–west, Fig. 2a) and plunges at 40–42° to the SW (203–218°) (Fig. 2b and c). It exposes a sheared contact with the Bulai pluton (Figs 1b, c and 2a; Holzer *et al*., 1998; van Kal, 2004; Perchuk *et al*., 2008*a*, 2008*b*; van Reenen *et al*., 2008, 2019; Smit *et al*., 2011). The dominant planar fabric preserved in supracrustal metapelites, calc-silicate rocks and quartzites defines the elliptical geometry of the structure (Fig. 2b; van Kal, 2004). Linear fabric is better preserved in micro-shear bands (e.g. sillimanite in metapelites, quartz and diopside in calc-silicate rocks, quartz in quartzites). All linear features display the same plunge direction as the core axis of the Ha-Tshanzi structure (Fig. 2c). The mineral stretching lineation is identical to that of other closed structures from different parts of the CZ (e.g. Bellevue and Avoca; Fig. 1b) as well as the NE-verging and SW-dipping Tshipise Straightening Zone. In contrast to the Bellevue and Avoca closed structures (Supplementary Materials Fig. S1; van Reenen *et al*., 2008), the Ha-Tshanzi structure was extensively overprinted by discrete north–south-trending shear zones at *c*. 2·01 Ga (e.g. Holzer *et al*., 1998) that resulted in disruption of earlier structures (note a spread of data points in Fig. 2b and c). However, the maximum density of the plotted linear elements defines exactly the same pole as for the Bellevue and Avoca structures (compare Fig. 2b and c with stereographic projections in Fig. S1 in Supplementary Materials; van Kal, 2004).

The Ha-Tshanzi structure shows an almost concentric arrangement of strata of various granulite-facies rocks (Fig. 2a). Meta-supracrustal rocks of the Beit Bridge Complex are dominant (Fig. 2a). Quartzites are located in the core of the structure, whereas intercalated discontinuous layers of migmatitic metapelites, amphibolites, quartzites, marbles and calc-silicate rocks are common at its periphery (Fig. 2a). Ultramafic lithologies, which are part of the Messina suite (Fig. 1c), are located in both the core and periphery of the Ha-Tshanzi structure. Leucocratic Singelele-type garnet-bearing granitoids occur in both the core and rim of the structure.

The studied metapelite sample LP19-11 (Fig. 3a) was collected from the western rim of the Ha-Tshanzi structure on the farm Tovi (22°19'55"S, 29°58'57"E; Fig. 2a) at the same general locality as

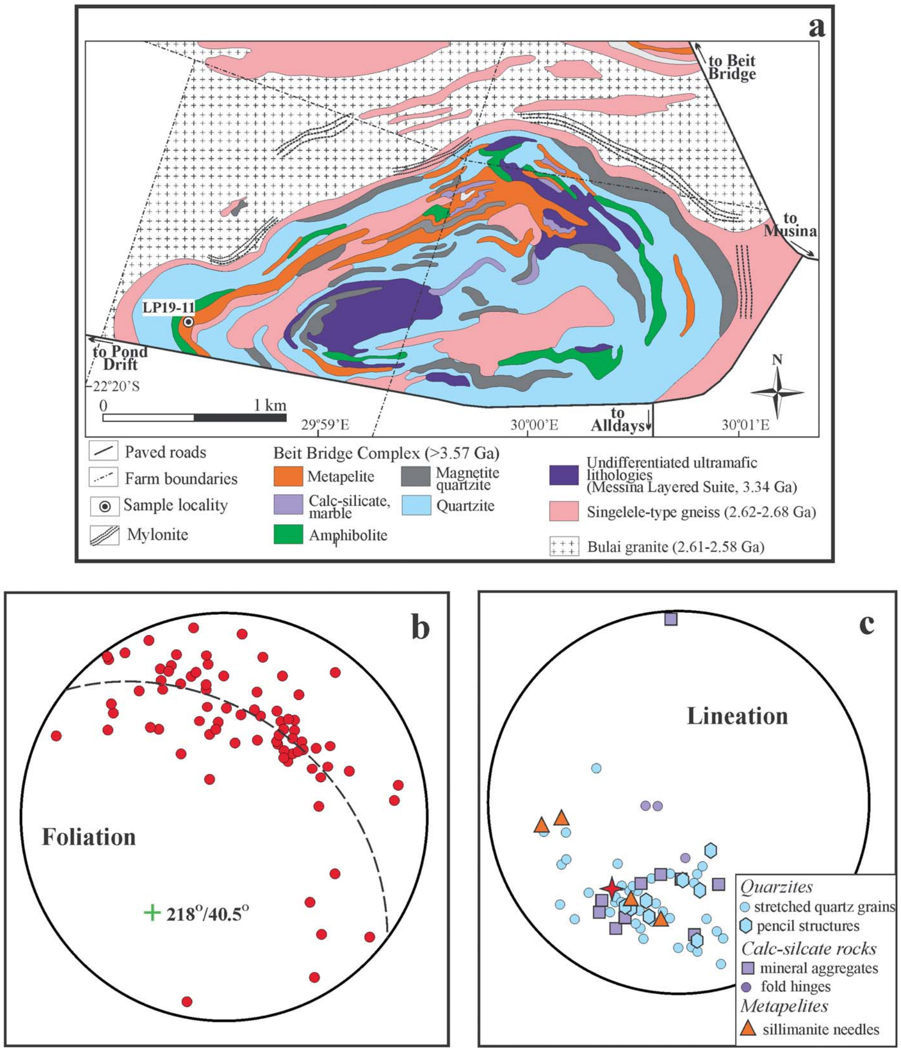

Fig. 2. Geological and structural characteristics of the Ha-Tshanzi closed structure. (a) Geological sketch map of the closed structure (after van Kal, 2004; Smit *et al*., 2011) showing the location of the studied sample LP19-11. (b) Stereographic southern hemispherical projection of foliation planes (red dots) around the entire Ha-Tshanzi structure; green cross at 218°/40·5° shows the central fold axis deduced from the poles to planes. (c) Stereographic southern hemispherical projection of linear elements around the entire Ha-Tshanzi structure for various rock types (see legend); red star corresponds to the central fold axis deduced from the poles to planes (218°/40·5°); the maximum density of lineations lies at 203°/42°. The poles to foliation planes define a great circle with a central fold axis (pole to the great circle) that coincides with the concentration of linear elements, thus defining the inclined cylindrical structure with the central fold axis plunging to the SW. The spread of the data points reflects an extensive overprint at 2·02 Ga (Holzer *et al*., 1998; van Kal, 2004).

that of sample TOV13 previously studied by van Kal (2004), Perchuk *et al*. (2008*b*) and Smit *et al*. (2011).

PETROGRAPHIC CHARACTERISTICS OF THE STUDIED METAPELITE

Structure, mineral assemblage and reaction textures

Metapelite LP19-11 is a garnet-rich, strongly banded and sheared gneiss (Fig. 3a–c). It comprises coarse-grained granoblastic garnet–biotite–quartzofeldspathic bands and lenses alternating with melanocratic Qz–Bt–Sil–Crd (mineral abbreviations are from Whitney & Evans, 2010) shear bands that crosscut both the matrix and garnet porphyroblasts (Fig. 3b and c). The attenuated shear bands have a protomylonitic texture, with variable preservation of garnet porphyroblasts (Fig. 3b and c). Garnet porphyroblasts vary from equant anhedral grains in the undeformed quartzofeldspathic bands (Figs 3b, c and 4a–c) to fish-shaped asymmetric porphyroblasts in the shear bands (Figs 3b, c and 4b). Some garnet porphyroblasts in the shear bands preserve a sigmoidal shape indicating movement along the shear planes (Figs 3b, c and 4a, b). However, such porphyroblasts are not abundant, and, thus, it is hard to identify the type of shearing (simple or pure shear) in the rock.

Both undeformed and deformed garnet porphyroblasts show inclusion-bearing cores and inclusion-poor peripheral zones (Figs 3b, c and 4a–c). The inclusions do not show any preferred orientation and are irregularly distributed in the garnet cores (Figs 3b, c and 4a–c). Despite attenuation of some porphyroblasts in the shear bands (Figs 3b, c and 4a, b), the inclusions in them are not oriented. This clearly indicates that garnet cores are pre-kinematic. The most common type of inclusion in garnet porphyroblasts is quartz. In many cases, quartz inclusions are euhedral or subhedral,

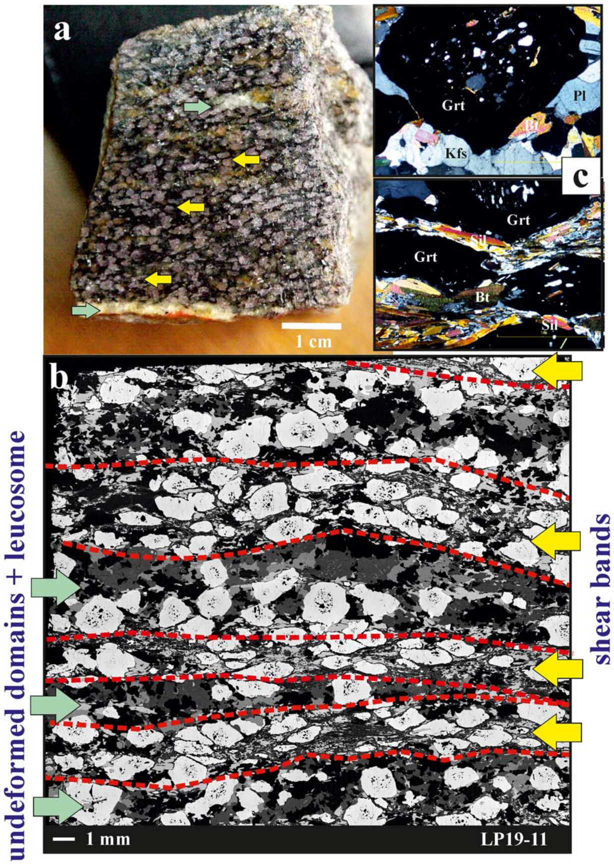

Fig. 3. General view of a hand-specimen (a) and BSE image of a representative thin section cut perpendicular to foliation (b) of metapelite sample LP19-11. The rock comprises undeformed coarse-grained garnet–biotite–quartz–feldspathic domains (indicated by light green arrows) and Bt–Sil–Crd–Qz-bearing shear bands that crosscut both matrix and the garnet porphyroblasts (indicated by yellow arrows). Garnet porphyroblasts in the undeformed quartzofeldspathic bands are equant anhedral grains, whereas they are strongly attenuated and deformed in the shear bands. Both undeformed and deformed garnet porphyroblasts show distinct cores crowded with inclusions and inclusion-poor peripheral zones. (c) Detailed optical images (cross-polarized light) of the coarse-grained garnet–biotite–quartz–feldspathic domain (upper image) and shear band enveloping garnet porphyroblasts (lower image). Orientation of sillimanite and biotite is clearly seen in the lower image. Horizontal scale of both images is 2 mm.

although rounded and anhedral inclusions are also common (Fig. 4c). Garnet also contains inclusions of apatite, monazite, rutile, zircon and rarely pyrrhotite, as well as polyphase inclusions (see below). In addition to biotite in the polyphase inclusions (Fig. 4c; see below), this mineral also forms rare individual inclusions in garnet. No sillimanite inclusions were found in cores of garnet porphyroblasts. However, small acicular inclusions of sillimanite (confirmed by Raman spectroscopy) are found in the peripheral zones of the garnet porphyroblasts in contact with the sillimanite-bearing shear bands (Fig. 4a–c).

The coarse-grained domains of the rock show a typical granitic texture with anhedral grains of plagioclase, quartz, and K-feldspar (Figs 3b, c and 4a–d). Disoriented biotite flakes of variable size are unevenly distributed in these domains. Biotite occurs both as individual flakes and at the edge of garnet (Fig. 4c). In addition to grains, K-feldspar forms lamellae-like ingrowths in plagioclase, as well as rims and microveins along plagioclase and quartz grain boundaries (Figs 3b and 4a–c). K-feldspar inclusions are absent in garnet. Cordierite grains are absent in the coarse-grained domains of the rock. Nevertheless, cordierite was found as thin rims around biotite flakes at their contacts with the quartzofeldspathic matrix (Fig. 4d). The rims contain prismatic inclusions of sillimanite, which, in turn, are mantled by sodic plagioclase (Fig. 4d). Graphite is disseminated along feldspar and quartz grain boundaries in the coarse-grained domains of the rock.

Cordierite, biotite, sillimanite and quartz form the shear bands (Figs 3b, c and 4a–c). No kyanite was identified using Raman spectroscopy. Shear bands are clearly distinguished by fine-grained aggregates of sillimanite needles, biotite flakes and attenuated grains of quartz, which are predominantly oriented parallel to the shear planes (Figs 3b, c and 4a, b; Supplementary Materials Fig. S2). Cordierite forms rims around biotite and sillimanite, and occurs at contacts of biotite with garnet. Plagioclase is rare, and K-feldspar is absent from the shear bands.

Polyphase inclusions in garnet

Polyphase inclusions are located among inclusions of quartz, apatite, monazite, zircon, rutile and rare individual inclusions of biotite in cores of garnet porphyroblasts (Fig. 4c). Polyphase inclusions are absent in the peripheral zones of the garnet porphyroblasts (Fig. 4c). Large (up to 300 μm) irregularly shaped inclusions are usually surrounded by numerous cracks (Fig. 5a and b). Some inclusions show a necking-down morphology and offshoots along the cracks filled with material like that in the main inclusions (Fig. 5b). These features are very similar to decrepitated melt inclusions reported in minerals from migmatitic rocks (e.g. Cesare *et al.*, 2015). Predominant phases in the polycrystalline inclusions are biotite, quartz, and plagioclase, as well as rare spinel, rutile and monazite. K-feldspar was not detected in the polyphase inclusions. Late cordierite was detected in one inclusion (Fig. 5b). Plagioclase in the polyphase inclusions looks spongy, with numerous small cavities (Fig. 5a), probably occupied by fluid inclusions. Cryptocrystalline material often accompanies the above minerals (Fig. 5a and b). Some smaller inclusions (less than 100 μm) containing quartz, and rarely biotite and plagioclase, show negative-crystal shape (Fig. 5a and b). These inclusions accompany larger ones (Fig. 5a and b) and might be interpreted either as individual inclusions or as accidentally exposed cross-sections of larger polyphase inclusions. In general, the textural features and phase composition of the inclusions are similar to those reported for ‘nanogranitic’ melt inclusions in peritectic minerals from migmatites (e.g. Cesare *et al.*, 2015; Bartoli *et al.*, 2016; Bartoli & Cesare, 2020).

In addition to the inclusions consisting of discernible crystalline aggregates, garnet contains inclusions of 10–50 μm in size filled with a cryptocrystalline material or aggregates of fibrous phases. Some inclusions are cored by quartz, or rarely rutile (Fig. 5a and c), whereas some others contain tiny, but visible, grains of apatite, monazite, sulfides, rutile, biotite and plagioclase. These inclusions usually show distinct negative crystal shape, characteristic of former melt inclusions (e.g. Cesare *et al.*, 2015; Bartoli *et al.*, 2016; Bartoli & Cesare, 2020; Fig. 5c). Their internal fibrous structure resembles so-called ‘supercooled melt inclusions’ (e.g. Hiroi *et al.*, 2014). Closer examination of euhedral quartz inclusions in garnet cores usually reveals rims of the cryptocrystalline or fibrous material around them. The K elemental maps of garnet porphyroblasts demonstrate a concentration of a dispersed K-rich material in the inclusion-rich cores

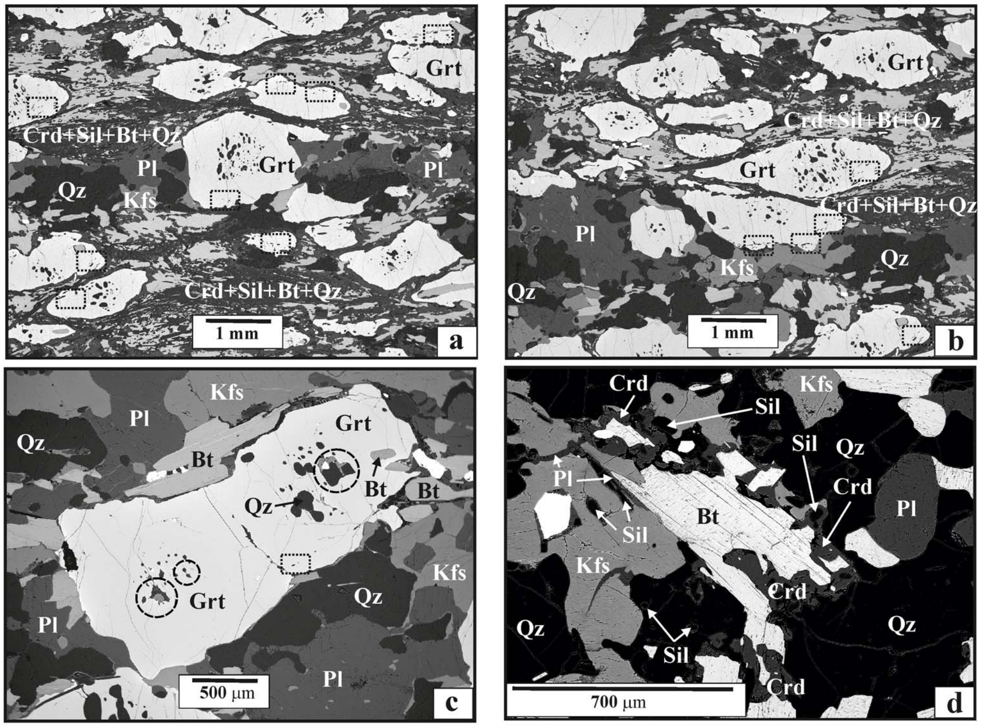

Fig. 4. Details of textural relationships in metapelite sample LP19-11. (a) Coarse-grained quartzofeldspathic lens with equant anhedral garnet grain surrounded by the Crd + Bt + Sil + Qz shear bands; garnet porphyroblasts in the shear bands are attenuated. (b) Strongly deformed attenuated fish-like garnet porphyroblasts streamlined and crossed by the Crd + Bt + Sil + Qz shears. (c) Equant garnet grains in the coarse-grained quartzofeldspathic domain; along with quartz inclusions, the grain cores contain polyphase inclusions (marked with dashed circles). Independent of their textural position, all porphyroblasts in (a)–(c) show inclusion-crowded cores and inclusion-poor peripheral zones. Along with anhedral K-feldspar grains, the quartz–feldspathic domains in (a)–(c) show K-feldspar microveins developed along the contacts of plagioclase and quartz. Dotted squares mark location of the sillimanite inclusions in the periphery of garnet porphyroblasts. Some garnet porphyroblasts contain individual inclusions of biotite. (d) Cordierite rims around a biotite flake in the coarse-grained quartz–feldspathic domain.

of the porphyroblasts (Fig. 5d). Thus, the euhedral quartz inclusions can also be interpreted as parts of partially crystallized semi-exposed melt inclusions.

ANALYTICAL PROCEDURES

Bulk-rock analysis

Sample LP19-11 of metapelite was crushed to a fine powder using a tungsten carbide swing mill. A glass disk was prepared for X-ray fluorescence (XRF) analysis as a mixture of high-purity fused anhydrous flux ($Li_2B_4O_7 + LiBO_2 + LiBr$), the rock powder (first dried at 105 °C) and $LiNO_3$. Volatiles were determined by loss on ignition. Whole-rock major element compositions were determined using a PW 2400 (Philips Analytical with SuperQ, PANalytical software) XRF system equipped with a robotic sample changer at the Institute of Geology of Ore Deposits, Petrography, Mineralogy and Geochemistry RAS (Moscow, Russia). Typical deviation from the reference value is less than 1 % for major elements present at a concentration of greater than 1 wt%. Measurements below 0·05 wt% were considered to be zero.

Trace element composition of the metapelite was analyzed using inductively coupled plasma mass spectrometry (ICP-MS) and inductively coupled plasma atomic emission spectrometry (ICP-AES) at the Analytical Certificate Testing Center of the Institute of Problems of Microelectronics and High-Purity Materials RAS (Chernogolovka, Russia).

BSE and microprobe analyses

Analyses of minerals were performed using the SEM Jeol 6480 LV equipped with an energy-dispersive spectrometry detector INCA-Energy 350 and wavelength-dispersive spectrometry detector INCA Wave 500 (Oxford Instruments) at the Laboratory of Local Methods of Analysis at the Department of Petrology of the Moscow State University. Analytical conditions were 15 kV acceleration voltage, 15 nA beam current, counting times of 100 s. The ZAF matrix correction was applied. Reintegration of compositions of perthitic K-feldspar was carried out using scanning over areas of 180–20 μm^2 depending on coarseness and density of plagioclase lamellae. Usually, zones with fine perthite lamellae (2–5 μm thick) were taken for reintegration. To estimate possible Na loss during analyses, counting times of 100 and 40 s were applied. It was found that scanning over areas does not produce measurable Na loss from alkali feldspar. Exposed areas of the polyphase (melt) inclusions also were analyzed using scanning over areas depending on the inclusion size.

The Jeol Superprobe JXA-8230 at the same laboratory was used to analyze both major elements and some trace elements (Ti, Sc, Y, P, Cr) in garnet. The analytical conditions were 20 kV acceleration voltage and 100 nA beam current. The slit size was 500 μm for all spectrometers. The garnet standards USNM 143968 (Mg-Kα_1, Al-Kα_1 and Si-Kα_1—TAP crystal; Fe-Kα_1—LiF crystal) and USNM 87375 (Ca-Kα_1—PET-J crystal) were used for calibration of the major elements (Jarosewich *et al*., 1980). Counting times for major elements were similar for both the standards and the sample: 40 s for Mg, Ca and Fe; 20 s for Al and Si. The dispersion of the measured

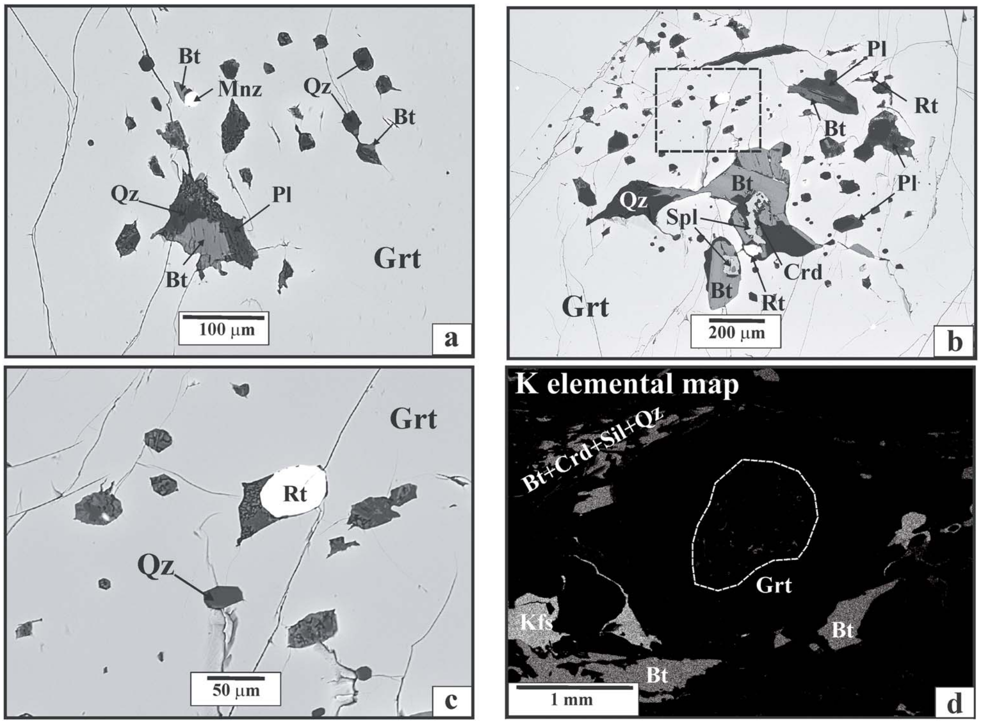

Fig. 5. Polyphase inclusions in garnet cores in the metapelite sample LP19-11. (a) Irregularly shaped biotite–plagioclase–quartz inclusion surrounded by smaller inclusions, some of which show a negative crystal shape; larger inclusion shows small offshoots; its upper portion is composed of the cryptocrystalline material; smaller inclusions consist of cores of euhedral quartz grains surrounded by the cryptocrystalline material. (b) Complex polyphase inclusion surrounded by smaller inclusions; dashed frame shows the position of (c). (c) Detailed view of small inclusions filled with cryptocrystalline and fibrous material; the clear negative crystal shape of the inclusions should be noted. (d) Elemental map showing distribution of potassium within the garnet porphyroblasts; dashed line marks the inclusion-rich core of the porphyroblast.

concentration during the major element analyses using the above conditions did not exceed 0·5 %. The following crystalline standards were used for the minor element analyses: $MnTiO_3$ for Ti-Kα_1 and Mn-Kα_1; Cr_2O_3 for Cr-Kα_1; $ScPO_4$ for P-Kα_1 and Sc-Kα_1; $Y_3Al_5O_{12}$ for Y-Lα_1. The Ti, Mn, Cr (crystal LiF) and P (crystal PET-J) measurements were performed using spectrometers with a 140 mm radius Rowland circle, whereas Sc and Y (crystal PET-H) were measured using a 100 mm radius H-type spectrometer. The position of maxima for the trace elements in garnets was specified by means of slow scanning of the corresponding spectral intervals. Counting time was set to attain the detection limit of 0·005 wt%: 30 s for Ti and Mn, 40 s for Cr, 60 s for P and Y, and 80 s for Sc. ZAF correction was applied to all analyses. Analytical conditions for the elemental mapping using the Jeol Superprobe JXA-8230 were the same as for individual spot analyses. Elemental maps with resolution 300 × 400 pixels were constructed on the basis of 24 scans with dwell time 20 ms at 20 kV acceleration voltage and 200 nA beam current. The obtained microprobe analyses are compiled in Tables S1–S6 in the Supplementary Materials.

Raman spectroscopy

Raman spectroscopy was applied for qualitative identification of Al-silicates included in garnet and in the shear bands, as well as for identification of volatiles (H_2O and CO_2) in cordierite. Measurements were performed using the JY Horiba XPloRa Jobin spectrometer equipped with a polarized Olympus BX41 microscope at the Department of Petrology and Volcanology, Moscow State University. Spectra were obtained using a 532 nm laser within the range 100–4000 cm^{-1} for 30 s. To better resolve the band of volatile species in cordierite, additional spectra were collected with longer exposure time within the ranges 1300–1400 and 3500–3600 cm^{-1}. The spectra were refined with LabSpec (version 5.78.24) software. Crystalline phases were identified using the rruff.info database. Volatile species in cordierite were identified using calibrations by Kolesov & Geiger (2000) and Haefeker *et al*. (2013).

Laser ablation multi-collector inductively coupled plasma mass spectrometry (LA-MC-ICP-MS)

Zircon, monazite and rutile grain fragments from the metapelites LP19-11 and TOV13 (Perchuk *et al*., 2008*b*) were handpicked after crushing and sieving using heavy liquids. After mounting and polishing, the zircons were imaged by cathodoluminescence (CL) on a Tescan SEM. Zircon, monazite and rutile were analyzed using LA-MC-ICP-MS on polished crystals utilizing an ASI RESOlution SE 193 nm Excimer laser ablation system equipped with a Nu Plasma II multi-collector ICP mass spectrometer, at the Spectrum Analytical Facility of the University of Johannesburg. All ablations consisted of a 15 s blank, and 40 s signal at a fluence of ~1·3 J cm^{-2}. Data reduction was done using an in-house Excel spreadsheet (Rosa *et al*., 2009), with common Pb corrections following to the crustal lead evolution line of Stacey & Kramers (1975). The Excel add-in Isoplot (v. 3.6; Ludwig, 2008) was used for age calculations.

For monazite, spots of 25 μm diameter were ablated at 6 Hz. The following reference materials were used for monazite: B0109

(1137 ± 1 Ma; Bingen *et al.*, 2008) and A276 (1916 ± 3 Ma; Y. Lahaye, pers. comm.). For zircon, spots of the same diameter were ablated at 1·6 Hz. Zircons GJ1 (608·5 ± 0·4 Ma; Jackson *et al.*, 2004), A382 (1877 ± 2 Ma; Huhma *et al.*, 2012) and OGC1 (3465·4 ± 0·6 Ma; Stern *et al.*, 2009) were used as reference materials. The reference material zircon CDQGNG measured as an unknown to check accuracy gave a weighted average $^{207}Pb/^{206}Pb$ age of 1847 ± 7 Ma (95 % confidence, $n = 10$; accepted age is 1851·5 ± 0·3 Ma; Schoene *et al.*, 2006). For rutile, spots of 60 μm diameter were ablated at 7 Hz. The reference material for rutile was rutile R632 (496 ± 2 Ma; Axelsson *et al.*, 2018). The Sugluk rutile gave 1711 ± 21 Ma (95 % confidence, $n = 7$; accepted age 1719 ± 14 Ma; Bracciali *et al.*, 2013) and rutile A49H gave 1873 ± 4 Ma [95 % confidence, $n = 5$; thermal ionization mass spectrometry (TIMS) age 1875 ± 3 Ma; Y. Lahaye, pers. comm].

MINERAL COMPOSITIONS

Biotite

Biotite exhibits wide variations of composition (Fig. 6a–c; Table S1, Supplementary Materials) in different textural positions of the mineral: (1) inclusions in garnet; (2) flakes in the quartzofeldspathic domains; (3) flakes in the shear bands.

Some visually individual biotite inclusions (Fig. 4a–c) are similar in composition to biotite from the polyphase inclusions (Fig. 5a and b) and probably represent semi-exposed polyphase inclusions. Nevertheless, most individual inclusions show lower $X_{Mg} = 0{\cdot}76$–$0{\cdot}78$, TiO_2 4·5–5·5 wt%, Cr_2O_3 0·23–0·27 wt% and Na_2O above 0·2 wt%, different from that of biotite in the polyphase inclusions (Fig. 6a–c; Table S1, Supplementary Materials). Biotite in the polyphase inclusions (Fig. 5a and b) shows the highest values of $X_{Mg} = 0{\cdot}79$–$0{\cdot}88$, and wide variations of TiO_2 of 5·1–0·0 wt%, which negatively correlate with X_{Mg} (Fig. 6a; Table S1, Supplementary Materials). In contrast to the individual inclusions, some biotite flakes in the polyphase inclusions are zoned with respect to TiO_2. Biotite in the polyphase inclusions is characterized by lower Cr_2O_3 (0·01–0·14 wt%) and V_2O_3 (0·02–0·20 wt%) contents. This biotite shows higher Na_2O content, 0·1–0·65 wt% (Fig. 6c; Table S1, Supplementary Materials), and Al_2O_3 content, 18·5–22 wt%. It is characterized by elevated content of Fe_2O_3 [calculated using the method by Li *et al.* (2020)], 0·8–2·8 wt%.

Some individual biotite inclusions in garnet are close in composition to biotite flakes in the quartzofeldspathic domains of the rock, implying that they belong to the same generation (Fig. 6a–c; Table S1, Supplementary Materials). Biotite flakes dispersed within the quartzofeldspathic domains show a relatively wide range of composition: $X_{Mg} = 0{\cdot}68$–$0{\cdot}76$, with TiO_2 content of 4–6·5 wt% (Fig. 6a; Table S1, Supplementary Materials). This type of biotite contains 0·3–0·4 wt% Cr_2O_3, 0·1–0·2 wt% Na_2O and <0·5 wt% Fe_2O_3 (Fig. 6b and c; Table S1, Supplementary Materials).

Compositions of this biotite partially overlap with compositions of biotite from the shear bands, which also show $X_{Mg} = 0{\cdot}65$–$0{\cdot}73$, $TiO_2 = 4{\cdot}8$–$6{\cdot}8$ wt%, $Cr_2O_3 = 0{\cdot}3$–$0{\cdot}6$ wt%, $V_2O_3 = 0{\cdot}18$–$0{\cdot}25$ wt%, and $Na_2O = 0{\cdot}05$–$0{\cdot}17$ wt% (Fig. 6a–c; Table S1, Supplementary Materials). Compositional overlap between the textural types of biotite suggests a genetic relation between them. Biotite in the shear bands shows the lowest Fe_2O_3 content.

All types of biotite are poor in halogens (Table S1, Supplementary Materials).

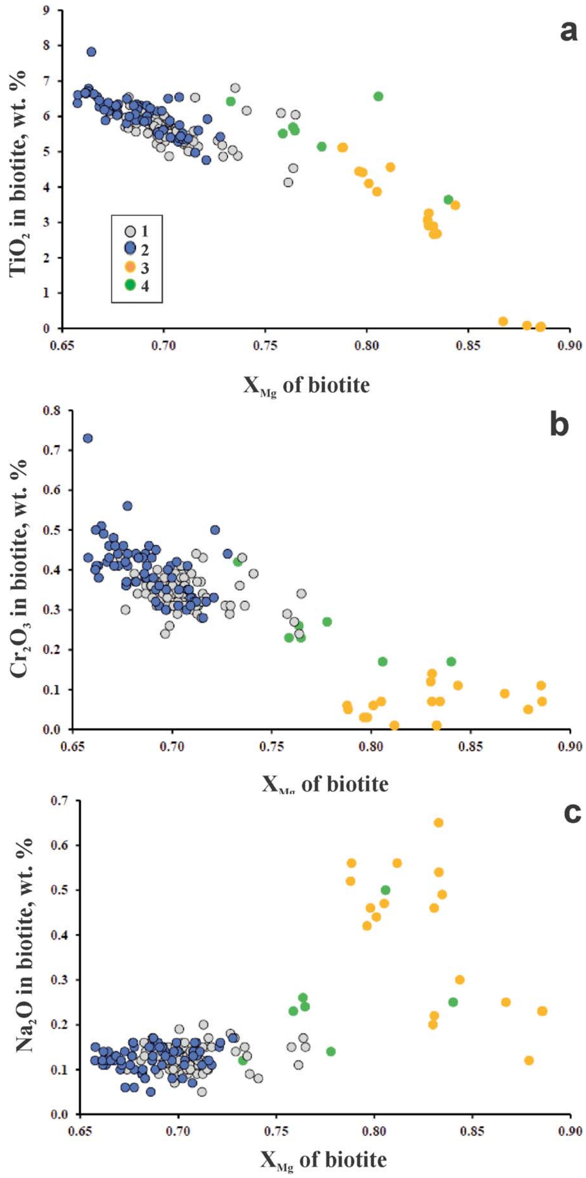

Fig. 6. Variations of biotite composition in the metapelite sample LP19-11 (Table S1 in Supplementary Materials). (a) X_{Mg} vs TiO_2; (b) X_{Mg} vs Cr_2O_3; (c) X_{Mg} vs Na_2O. 1, Biotite in the coarse-grained quartz–feldspathic domains; 2, biotite in the shear bands; 3, biotite in the polyphase inclusions in garnet; 4, individual biotite inclusions in garnet.

Cordierite

Cordierite in the shear bands shows $X_{Mg} = 0{\cdot}85$–$0{\cdot}90$ (Table S2, Supplementary Materials), which usually increases by 2–3 mol% toward contacts with garnet. Cordierite rims on biotite flakes in the quartzofeldspathic domains (Fig. 3d) are less magnesian, $X_{Mg} = 0{\cdot}84$–$0{\cdot}85$ (Table S2, Supplementary Materials). Cordierite with $X_{Mg} = 0{\cdot}89$ (Table S2, Supplementary Materials) was found in one polyphase inclusion in garnet as a rim between biotite and spinel (Fig. 5b).

Raman spectra of cordierite from the shear bands (Fig. S3, Supplementary Materials) show clear bands at ∼1383 cm^{-1}, assigned to $2\nu 2$ vibration modes of CO_2, and at ∼3597 cm^{-1}, reflecting the class I H_2O molecule vibrations (Kolesov & Geiger, 2000; Haefeker *et al.*, 2013). Applying the updated equations of the dependences of

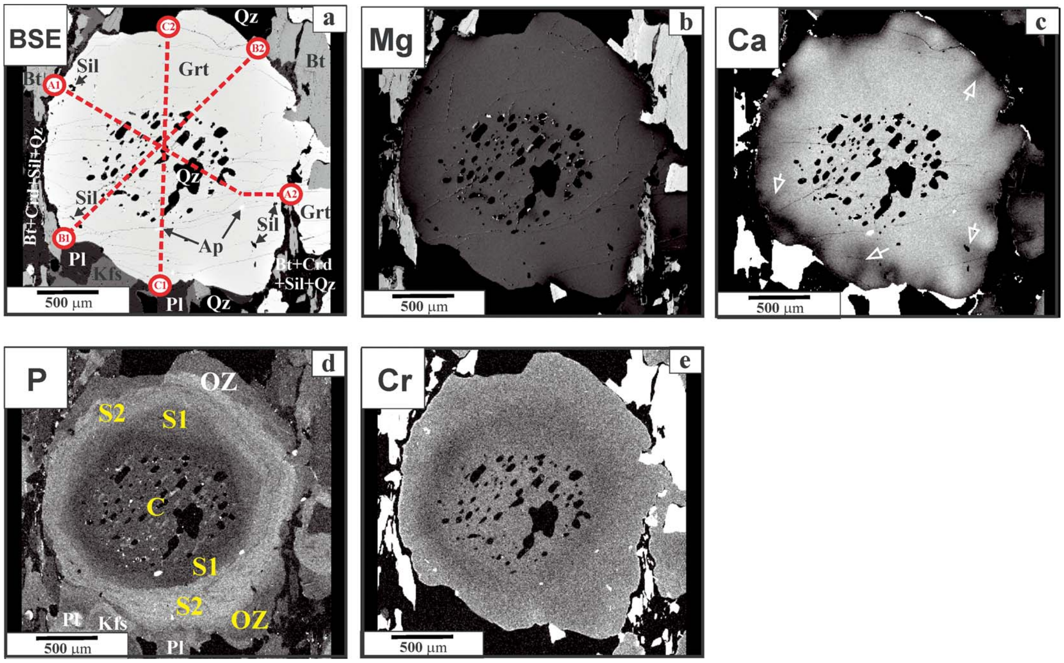

Fig. 7. Zoning of an equant undeformed garnet in the quartz–feldspathic domain. (a) BSE image of the garnet showing profiles A1–A2, B1–B2 and C1–C2 described in the text. (b) Mg elemental map of the garnet. (c) Ca elemental map of the garnet; open arrows show low-Ca stringers. (d) P elemental map of the garnet and adjacent minerals (note relatively high content of P in feldspars surrounding garnet). (e) Cr elemental map of the garnet; bright spots in the outer zone of the garnet are inclusions of Cr-bearing sillimanite.

the intensities of the bands I_{1383}/I_{970} and I_{1383}/I_{1180} with the CO_2 concentration in cordierite (Haefeker *et al*., 2013), 1·1–1·3 wt% CO_2 was estimated. This content corresponds to 0·15–0·18 molecules of CO_2 per formula unit normalized to 18 oxygen atoms.

Spinel

Spinel found in the polyphase inclusions (Fig. 5b) shows X_{Mg} = 0·54–0·56, and contains ~6 wt% ZnO, ~0·4 wt% Cr_2O_3, and ~0·2 wt% of both CoO and NiO.

Al-silicate

Raman spectroscopy confirmed the Al-silicate in the metapelite as sillimanite. Acicular inclusions of this mineral in garnet periphery zones (Fig. 4a–c) contain 0·59–0·85 wt% FeO and 0·2–0·33 wt% Cr_2O_3 (Table S3, Supplementary Materials). Sillimanite crystals in shear bands contain lower (0·24–0·36 wt%) FeO and similar concentrations of Cr_2O_3 (Table S3, Supplementary Materials).

Plagioclase

The composition of anhedral grains of plagioclase coexisting with K-feldspar and quartz in the coarse-grained domains of the rock (Figs 3b and 4a–d) varies within the range X_{Ca} = 0·26–0·36 (Fig. S4 and Table S4, Supplementary Materials). However, plagioclase with X_{Ca} above 0·29 commonly occurs along the contact with K-feldspar microveins and rims, suggesting that a slight increase of the anorthite content in plagioclase is related to the later operation of Korzhinskii's reaction controlled by an increase of K activity in a fluid (e.g. Aranovich & Safonov, 2018). Thus, the initial composition of plagioclase in the coarse-grained domains is limited to X_{Ca} = 0·26–0·28 (Fig. S4, Supplementary Materials).

Plagioclase in the shear bands intergrown with cordierite, biotite, sillimanite and quartz shows higher X_{Ca} = 0·29–0·35 (Fig. S3 and Table S4, Supplementary Materials). Overlap of compositions with plagioclase from the coarse-grained domains (Fig. S3, Supplementary Materials) indicates that plagioclase in the shear bands is reworked matrix plagioclase.

Plagioclase in polyphase inclusions (Fig. 5a and b) is the most Na-rich one, X_{Ca} = 0·10–0·21 (Table S4, Supplementary Materials), reflecting crystallization from the trapped silicate melt.

K-feldspar

$X_K = K/(K + Na + Ca + Ba)$ of K-feldspar lamellae ingrowths in matrix plagioclase varies within the range 0·89–0·94 (Table S4, Supplementary Materials). Large K-feldspar grains in the coarse-grained domains usually contain small perthitic lamellae. Integrated analyses show that these K-feldspar grains are relatively homogeneous, with X_K = 0·85–0·86 (Table S4, Supplementary Materials). Usually, K-feldspar usually contains 0·5–0·6 wt% BaO, as well as up to 0·1 wt% P_2O_5 (Table S4, Supplementary Materials).

GARNET ZONING

Zoning of undeformed garnet porphyroblasts

Three profiles labelled A1–A2, B1–B2, and C1–C2 (Fig. 7a; Table S5, Supplementary Materials) and elemental maps (Fig. 7b–e) are constructed for an equant garnet grain in the quartzofeldspathic domain of the metapelite to characterize the zoning of garnet with respect to major and minor elements prior to the shear deformation. This grain is slightly touched by small shear bands (expressed in elongated crystals of sillimanite and biotite flakes) that are adjacent to the grain on the left and right. The shear band on the right detaches

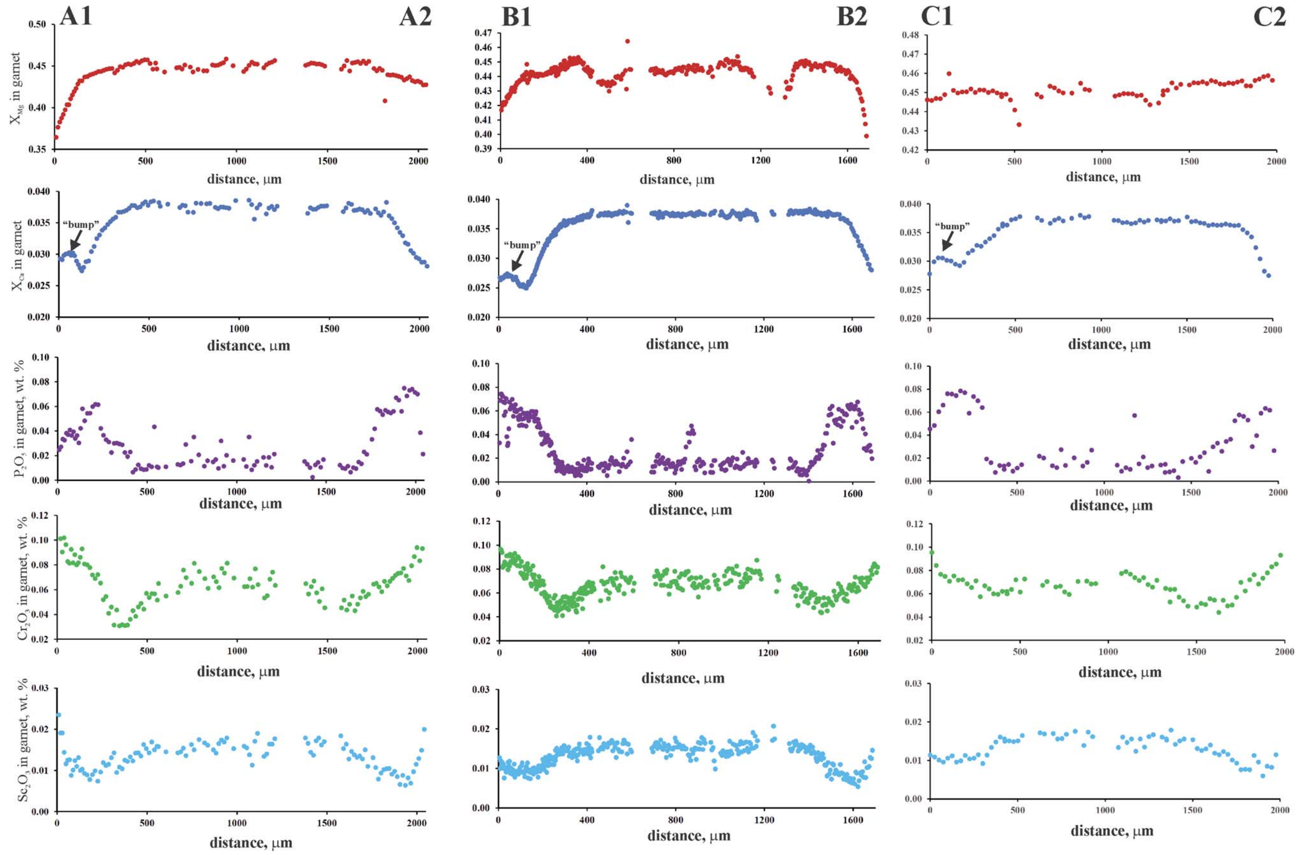

Fig. 8. Profiles A1–A2, B1–B2 and C1–C2 of an equant garnet in the quartz–feldspathic domain (Fig. 6a) with respect to X_{Mg} (first row of profiles), X_{Ca} (second row), and contents of P_2O_5 (third row), Cr_2O_3 (fourth row) and Sc_2O_3 (fifth row).

a small piece of garnet from the main grain. Profile A1–A2 (Fig. 7a), bounding the edges of the garnet grain in contact with the shear bands (Fig. 8), shows X_{Mg} = 0·44–0·45 in the inclusion-rich core with only local variations at the contacts with the inclusions (Table S5, Supplementary Materials). The profile is asymmetric with a slight decrease down to 0·43 observed at the right edge of the profile, whereas it drops down to 0·36–0·37 at the left edge (Fig. 8). Profile B1–B2 (Fig. 7a), the edges of which are in contact with large biotite flakes, shows a near-symmetric decrease of X_{Mg} down to 0·40–0·41 at both edges (Fig. 8; Table S5, Supplementary Materials). In contrast, the X_{Mg} values along the profile C1–C2 (Fig. 7a), which bounds garnet edges at contacts with the unsheared quartzofeldspathic matrix, vary around 0·45, with only local fluctuations at the contact inclusions, with no decrease of X_{Mg} at the edges (Fig. 8; Table S5, Supplementary Materials). The Mg elemental map of the garnet grain (Fig. 7b) clearly shows that (darkened) lower-Mg zones are restricted to the contacts with the shear bands and also form local pockets at the contacts with biotite but are absent at the contacts with the unsheared quartzofeldspathic matrix.

Behavior of X_{Mn} is very similar to that of X_{Mg}. The X_{Mn} values are constant at ~0·01 in cores of the garnet grain, but slightly increase at rims. However, an increase of X_{Mn} is absent at the contacts with the unsheared quartz–feldspathic matrix (i.e. along the profile C1–C2).

In contrast to X_{Mg}, profiles of X_{Ca} look symmetric (Fig. 8; Table S5, Supplementary Materials), with X_{Ca} varying from 0·037–0·038 in the inclusion-bearing cores to 0·026–0·030 in rims (Fig. 8). The X_{Ca} values start to decrease almost immediately beyond the limits of the inclusion-bearing cores. Variations of X_{Mg} and X_{Ca} are not coupled (Fig. 8). Despite a relative constancy of X_{Mg} (0·44–0·45) in the profile C1–C2, X_{Ca} decreases (Fig. 8). The X_{Ca} profiles show 'bumps' of 50–100 µm width, indicating some local garnet inhomogeneities at the edges (Fig. 8).

The Ca elemental map (Fig. 7c) clarifies the fact that Ca zoning is not concentric. Low-Ca areas form bays and appendages at the edges of the garnet grains. Some of them have linear morphology oriented toward the garnet core. Wedge-like appendages indicate that some low-Ca domains appear to be formed as fractures in the higher-Ca garnet and, subsequently, were healed by lower-Ca garnet material. The 'bumps' at the ends of the Ca-zoning profiles (Fig. 8) represent the higher-Ca garnet 'relics' detached from the main grain by lower-Ca domains. Locally, sillimanite and quartz inclusions are attached to the low-Ca domains and appendages (Fig. 7c). The low-Ca domains are not attached exclusively to the garnet edges adjacent to the shear bands, but are also developed along the edges in contact with the undeformed quartzofeldspathic matrix (Fig. 7c). X_{Ca} of garnet in the low-Ca domains and appendages is generally below 0·03. They are not expressed in terms of X_{Mg} (compare Fig. 7b and c). In contacts with the quartzofeldspathic matrix, X_{Mg} of the the low-Ca domains and appendages is 0·44–0·45; that is, similar to X_{Mg} of the central zones of garnet grain.

The elemental map in Fig. 7d shows concentric zoning of the garnet with respect to phosphorus. The euhedral hexagonal core crowded with inclusions (C) shows the lowest P_2O_5 content

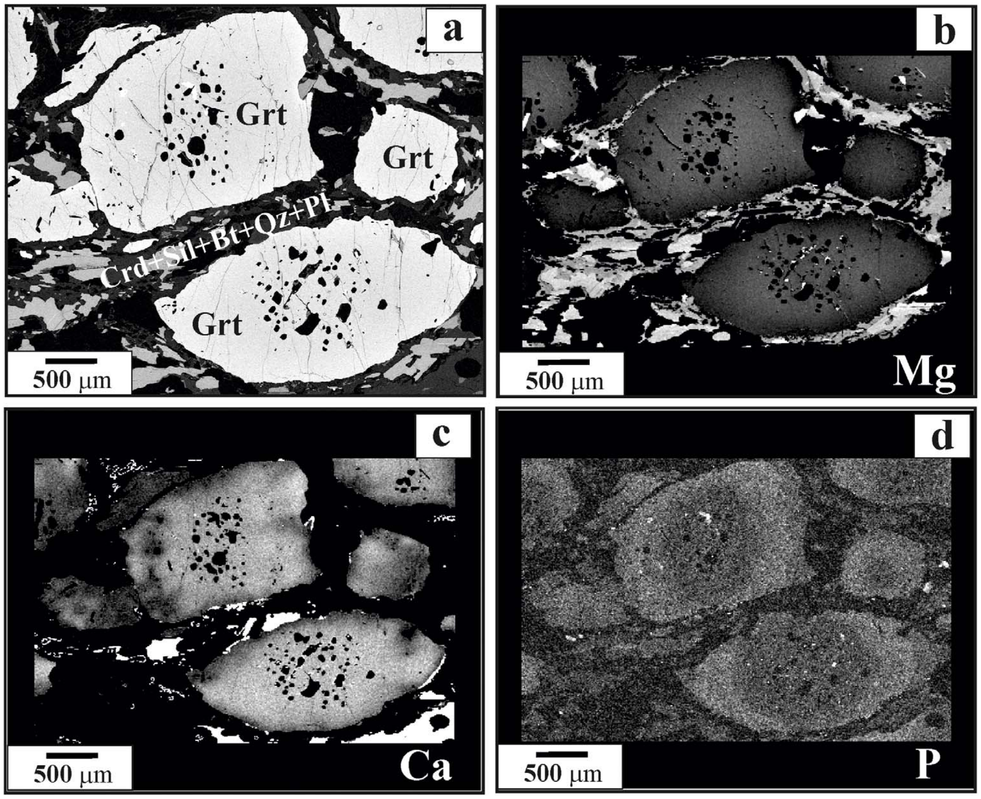

Fig. 9. Zoning of weakly deformed garnet grains trapped by the shear bands. (a) BSE image. (b) Mg elemental map. (c) Ca elemental map. (d) P elemental map.

(0·01–0·02 wt%) in all three profiles (Fig. 8). The core contains inclusions of phosphorus-bearing phases (Fig. 7d). Apatite is a common inclusion, but monazite is also present. The core is overgrown by a euhedral intermediate zone with higher P_2O_5 content (Fig. 7d), which consists of at least two distinct shells characterized by different P_2O_5 contents (S1 and S2). The maximal P_2O_5 content 0·06–0·07 wt% is reached in shell S2 (Fig. 8). These shells contain only rare apatite inclusions (Fig. 7d). The C–S1 and S1–S2 interfaces do not show evidence for resorption, and transition between these zones is gradual (Fig. 7d). The shell S2 is followed by a low-P outer zone (OZ), where P_2O_5 content drops to 0·02 wt%. An interface between S2 and OZ is uneven and the outer zone is not continuous (Fig. 7d). It is better developed at the contacts with the unsheared quartzofeldspathic matrix, but is almost absent at contacts with the shear bands (Fig. 7d), suggesting that the P-zoning of garnet was strongly eroded during formation of the shear bands.

The Cr zoning is also concentric and symmetric with a clear euhedral core (inclusion-rich) containing up to 0·08 wt% Cr_2O_3, a low-Cr (0·03–0·05 wt% Cr_2O_3) relatively narrow intermediate shell and a high-Cr (0·09–0·10 wt% Cr_2O_3) wide outer zone (Fig. 8). The elemental map (Fig. 7e) shows that, in contrast to other zones, the outer zone contains small inclusions of Cr-bearing sillimanite. Unlike P-zoning (Fig. 8), the Cr-zoning seems to be not affected by the shear bands. Zoning with respect to Sc_2O_3 (Fig. 8) in general repeats the zoning with respect to Cr_2O_3, outlining the core, the intermediate shell and the outer zone.

Concentration of TiO_2 in the garnet (Table S5, Supplementary Materials) varies within the range 0·015–0·035 wt%, but without any specific zoning.

Zoning of garnet porphyroblasts modified by shearing

Figure 9a–d shows elemental maps of garnet grains located within the shear bands. These garnet grains are characterized by wide darkened low-Mg zones along the entire perimeter of the grains (Fig. 9b). The map of a porphyroblast in the lower portion of Fig. 9c shows a relatively homogeneous distribution of Ca in the inclusion-bearing core, but irregular low-Ca rims at the contacts with the shear bands (Fig. 9c). Other porphyroblasts in this figure have a complex spotty pattern of Ca-zoning, which evidently was created by strong fracturing and subsequent healing of garnet grains. The low-Ca areas contain small inclusions of sillimanite. The complete initial shell-like phosphorus-zoning, similar to the zoning in Fig. 7d, is preserved just along the longest axis of the porphyroblasts roughly oriented along the shear plane, but is strongly disturbed and destroyed at the contacts with the shear bands (Fig. 9d).

Complex heterogeneity is revealed by highly deformed attenuated garnet porphyroblasts (Fig. 10a–f). Low-Mg zones are developed on the entire perimeter of the grains (Fig. 10c), whereas higher-Ca domains in these garnets are preserved as relics (Fig. 10d). Unlike the undeformed porphyroblast (Fig. 9a), the inclusion-bearing cores of these attenuated porphyroblasts show low Ca content (are darker in the elemental maps; Fig. 10d). In our opinion, this feature does not reflect the initial composition of the cores, but rather a strong modification of the porphyroblasts via fracturing and subsequent healing by the low-Ca garnet material. This conclusion follows from the fact that the cores are connected to the low-Ca rims by channels crossing higher-Ca domains (see white arrows in Fig. 10d). The relics preserve X_{Ca} = 0·036–0·037, which is characteristic for the core portions of the large undeformed garnet grains (Fig. 8). The channels

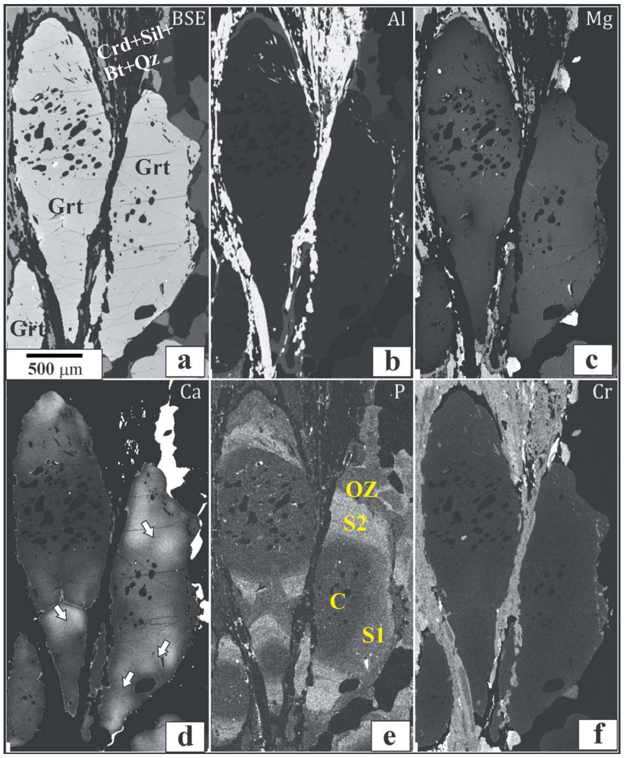

Fig. 10. Zoning of strongly deformed attenuated garnet grains trapped by the shear bands. (a) BSE image. (b) Al elemental map. (c) Mg elemental map. (d) Ca elemental map (white arrows show low-Ca channels connecting cores of the porphyroblasts with the outer zones). (e) P elemental map (note that the preserved zoning C–S1–S2–OZ in the right-hand porphyroblast repeats the zoning of the undeformed grain in Fig. 6d). (f) Cr elemental map.

show X_{Ca} = 0·033–0·032, whereas the lowest values, X_{Ca} = 0·026–0·027, are characteristic of the contacts with the shear bands. Zoning with respect to P is extremely disturbed by plastic deformation of the grains and is destroyed at the contacts with the shear bands (Fig. 10e). The undisturbed initial zoning is very locally preserved and clearly repeats the zoning pattern (C–S1–S2–OZ) of the undeformed grain (Fig. 7d). Zoning with respect to Cr appears to be similar (Fig. 10f).

COMPOSITION OF THE POLYPHASE INCLUSIONS

The composition of the exposed areas of the relatively large (20–50 μm) inclusions with euhedral shapes filled with cryptocrystalline and fibrous material (Fig. 5a and c) was measured via rastered microprobe analyses (Table S6, Supplementary Materials). The contribution of the garnet composition to the rastered analysis has been estimated for the inclusions by means of a series of analyses over various areas either including or not including garnet. For comparison, this procedure was repeated for the exposed euhedral quartz inclusions in garnet of a size comparable with the size of the melt inclusions (20–40 μm). Figure 11a–d presents analyses of the inclusions (Table S6, Supplementary Materials) that do not contain visible mineral grains.

The analyses (normalized to 100 wt% from Table S6 in Supplementary Materials) show a variation of SiO_2 from 54 to 81 wt%. The SiO_2 content shows a negative correlation with Al_2O_3 and MgO + FeO (Fig. 11a and b), which positively correlate with each other (compare Fig. 11a and b). Such correlation is related to variable contamination by 'garnet component' in the measured areas. In turn, inclusions with high SiO_2 (up to 80 wt%) seem to be the result of contamination with quartz. The inclusions are characterized by widely varying $K_2O + Na_2O$ (<1 to 8 wt%) and CaO (<0·1 to 2 wt%) contents without any correlation with SiO_2 (Fig. 11c and d; Table S6 Supplementary Materials). Measured inclusions are peraluminous, with ASI [= molar $Al_2O_3/(K_2O + Na_2O + CaO - 1{\cdot}67P_2O_5)$] significantly higher than 1·1. Values up to 3–5 correspond to measured areas of the inclusions depleted in alkalis, but rich in MgO + FeO along with Al_2O_3; that is, strongly affected by the 'garnet component'. Many measured exposed areas of the inclusions demonstrate 1–4 wt% P_2O_5, which usually correlates with the CaO content, suggesting compositional influence of apatite. However, even areas that do not expose any visible apatite show up to 0·2–0·3 wt% P_2O_5 (Table S6, Supplementary Materials).

WHOLE-ROCK GEOCHEMISTRY OF THE METAPELITE

The bulk composition of the metapelite sample LP19-11 (wt%) is as follows: SiO_2 56·30, TiO_2 0·84, Al_2O_3 18·58, FeO 11·63 (recalculated from 12·93 wt% Fe_2O_3 measured by XRF), MnO 0·17, MgO 7·24, CaO 0·85, Na_2O 0·62, K_2O 1·68, P_2O_5 0·03, loss on ignititon (LOI) 0·37. The composition is comparable with that of high-Al metapelites distinguished by Boryta & Condie (1990) and Rajesh *et al.* (2018*b*) in different parts of the CZ (Fig. 12a–c). However, sample LP19-11 is richer in MgO + FeO and lower in Al_2O_3. The composition of the studied sample is also close to that of metapelite samples studied by Millonig *et al.* (2008), and sample TOV13 studied by Perchuk *et al.* (2008*b*) from the same locality in the Ha-Tshanzi structure, although this sample is richer in silica (Fig. 12a–c). The chondrite-normalized rare earth element (REE) pattern of the Ha-Tshanzi metapelite (Fig. 12d) is comparable with that of low-Al metapelites (Boryta & Condie, 1990), but shows an increase of heavy REE (HREE) up to the level of high-Al metapelites (Fig. 12d) reflecting the enrichment of the rock in garnet (Fig. 3a and b).

P–T CONDITIONS

Phase equilibria modeling

Phase equilibria modeling for the above bulk composition of the metapelite sample LP19-11 was performed via the Gibbs free energy minimization in the system MnO–Na_2O–CaO–K_2O–FeO–MgO–Al_2O_3–SiO_2–H_2O–TiO_2–O_2 (MnNCKFMASHTO) using the PERPLE_X software (Connolly, 2005) in version 6.7.7 for Windows (http://www.perplex.ethz.ch). The standard properties database hp11ver.dat (i.e. Holland & Powell, 2011) was applied for modeling. The following models from White *et al.* (2014) were applied for mineral solutions (see http://www.perplex.ethz.ch/perplex/datafiles/solution_model.dat): Crd(W) for hydrous Fe–Mg–Mn cordierite, Gt(W) for Fe^{3+}-bearing Ca–Mg–Fe–Mn garnet, and Bi(W) for Ti- and Fe^{3+}-bearing biotite. The model 'feldspar' based on the solution model of Fuhrman & Lindsley (1988) was taken for ternary feldspar and model Ilm(WPH) was applied for the ilmenite solid solution (White *et al.*, 2000). The model melt(W) from White *et al.* (2014) was used for the NCKFMASH silicate melt.

Absence of Fe_2O_3 in garnet, very low content of Fe_2O_3 in biotite (just 0·2–0·3 wt% on average), and presence of rutile, pyrrhotite and pentlandite indicate low oxidation state of the metapelite sample.

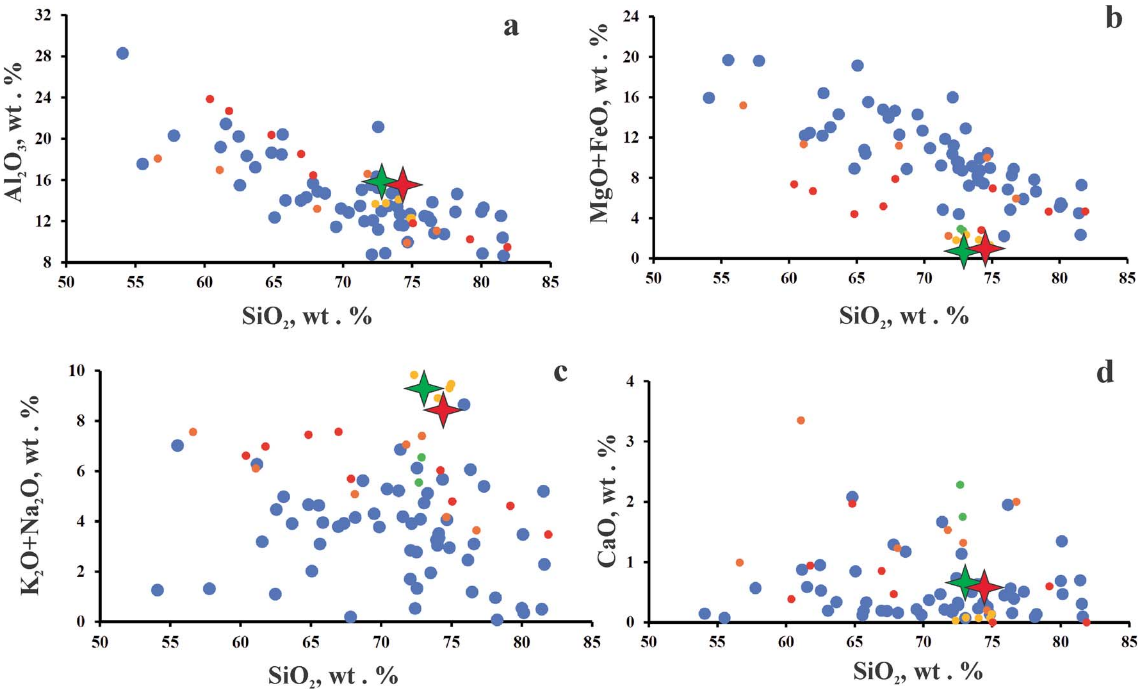

Fig. 11. Composition (normalized to 100 %) of the exposed areas of the inclusions filled with cryptocrystalline and fibrous material (blue large circles). Analyses are taken from Table S6 in Supplementary Materials. (a) Negative correlation of SiO_2 and Al_2O_3 in the inclusions. (b) Negative correlation of SiO_2 and MgO + FeO in the inclusions. (c) Variations of $K_2O + Na_2O$ in the inclusions. (c) Variations of CaO in the inclusions. Four-pointed stars show compositions of melts estimated from PERPLE_X at 820 °C/10·2 kbar (green) and 780 °C/7·1 kbar (red). Small colored circles show composition of melts produced in some experiments on partial melting of peraluminous metapelites: orange, Koester *et al.* (2002), anhydrous melting of a cordierite-bearing metapelite at 10 kbar; green, Koester *et al.* (2002), melting of a cordierite-bearing metapelite in presence of additional 5 wt% H_2O at 10 kbar; yellow, Carrington & Harley (1995), anhydrous melting of a model metapelite Bt + Sil + Qz + Kfs + Grt at 7–12·5 kbar; red, Le Breton & Thompson (1988), anhydrous melting of a natural metapelite Bt + Ky + Qz + Kfs + Grt at 10 kbar.

Therefore, the pseudosection (Fig. 13a) was computed at the arbitrary 'free' O_2 (as a monitor of Fe_2O_3) content 0·005 wt%. The optimal H_2O content in the system (M_{H2O}) was specified from the best convergence of isopleths of mineral composition ($X_{Mg}{}^{Grt}$, $X_{Ca}{}^{Grt}$, $X_{Mg}{}^{Bt}$, $X_{Mg}{}^{Crd}$, $X_{Ca}{}^{Pl}$) on the T–M_{H2O} and P–M_{H2O} pseudosections and was found to be ~1 wt%.

The pseudosection (Fig. 13a) is subdivided into the cordierite-absent portion above ~7·5 kbar and the cordierite-bearing portion below ~7·5 kbar. In both portions, melt coexists with Grt + Bt + Sil(Ky) + Pl + Qz + Rt. The solidus shows a ledge at ~6·5 kbar (Fig. 13a), along which the solidus temperature increases with insignificantly decreasing pressure by ~50 °C. This ledge is related to the appearance of cordierite at pressures below ~7·5 kbar. Cordierite sequesters water, thus inhibiting melting (e.g. Stevens *et al.*, 1995). Calculations furthermore show that the ledge extends to higher temperatures with decreasing water content in the system.

Figure 13b shows isopleths for $X_{Mg}{}^{Grt}$ = 0·44–0·45 and $X_{Ca}{}^{Grt}$ = 0·036–0·038, which are characteristic for the garnet cores, $X_{Ca}{}^{Pl}$ = 0·26–0·28 for plagioclase, and $X_{Mg}{}^{Bt}$ = 0·75–0·76, which is the maximal Mg-number for the individual biotite flakes, from the coarse-grained domains of the rock. These compositions of the minerals are considered to reflect peak metamorphic conditions for the sample LP19-11. A closer superimposition of the isopleths corresponds to a pressure of ~10·2 kbar and temperature 810–830 °C (area Ia in Fig. 13b). Taking into account that the starting $X_{Mg}{}^{Grt}$ could have been be slightly higher (~0·46), the temperature range can be extended up to 850 °C. The estimated P–T parameters are at the kyanite–sillimanite boundary (Fig. 13a). Although relic kyanite has been reported in metapelitic granulites of the CZ (Zeh *et al.*, 2004), this phase was not identified in the studied sample. At the above conditions, the assemblage Grt + Bt + Pl + Qz + Sil (Ky) + Rt coexists with 9–11 vol% of a melt (Fig. 13d) of the following average composition (wt%): SiO_2 66·9, Al_2O_3 14·9, FeO 0·5, MgO 0·2, CaO 0·7, Na_2O 4·3, K_2O 4·3, H_2O 8·2 (see green four-pointed star in Fig. 11a–d, normalized to water-free basis).

Area Ib (Fig. 13b) at pressure ~7·5 kbar and temperature similar to the peak ones, 810–830 °C, indicates a superimposition of isopleths $X_{Mg}{}^{Grt}$ = 0·44–0·45 and $X_{Ca}{}^{Grt}$ = 0·030–0·028, which is characteristic for the lower-Ca domains and channels at the edges of garnet grains (Fig. 7c). This area is situated at the boundary separating the Crd-free and Crd-bearing phase fields (Fig. 13a) and, thus, marks the P–T condition at which cordierite begins to form in the metapelite. As cordierite forms, modes of garnet (+ Sil + Qz) begin to drastically decrease, indicating reaction (e.g. Aranovich & Podlesskii, 1989):

$$\frac{1}{3}\mathrm{Grt} + \frac{2}{3}\mathrm{Sil} + \frac{5}{6}\mathrm{Qz} = \frac{1}{2}\mathrm{Crd}. \quad (1)$$

However, it cannot be excluded that cordierite forms via reactions of earlier garnet and biotite with the residual melt [see possible variants given by Weinberg & Hasalová (2015)]. The cordierite rims around biotite (Fig. 4d) in the leucosome domains seem to be a good representation of this process.

Superimposition of isopleths for $X_{Mg}{}^{Grt}$ = 0·36–0·42, $X_{Ca}{}^{Grt}$ = 0·026–0·030, $X_{Ca}{}^{Pl}$ = 0·30–0·35, $X_{Mg}{}^{Bt}$ = 0·67–0·73 and $X_{Mg}{}^{Crd}$ = 0·84–0·88, which characterize variations of mineral compositions within the shear bands, corresponds to pressure of ~7·2 kbar and

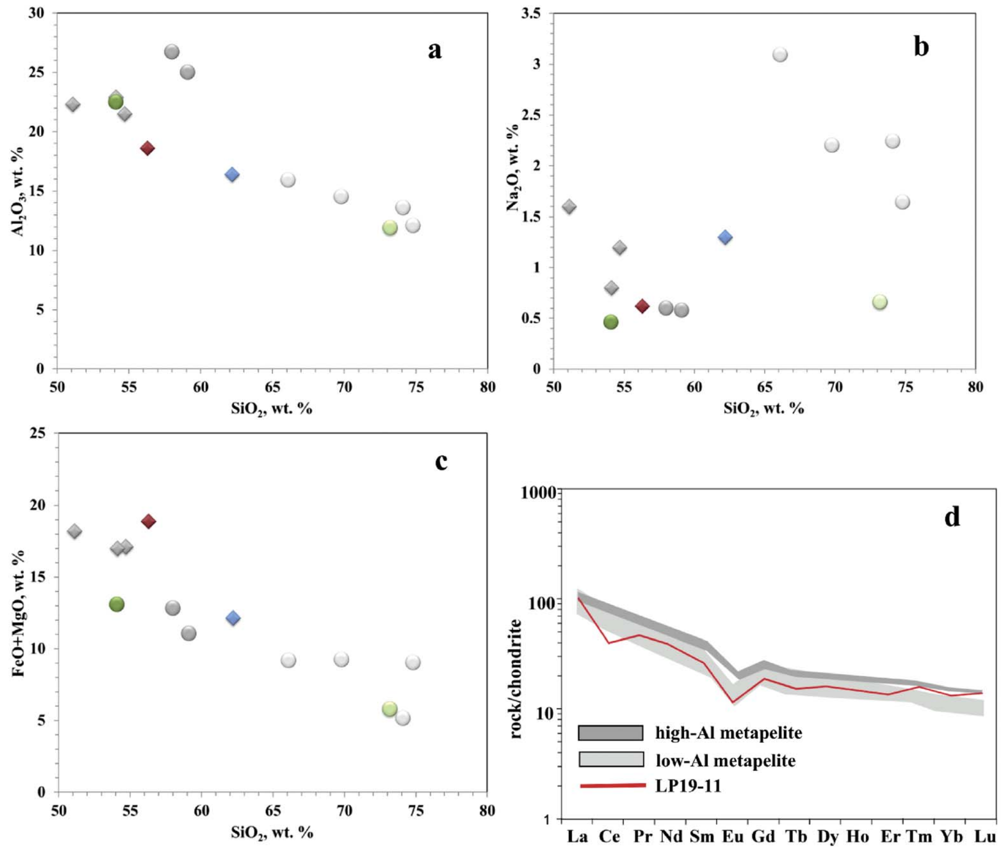

Fig. 12. Whole-rock chemistry of the metapelite sample LP19-11 (dark red diamond) in comparison with the composition of high-Al metapelites (dark grey circles) and low-Al metapelites (light grey circles) distinguished by Boryta & Condie (1990) in the Musina area of the CZ: (a) SiO_2–Al_2O_3, (b) SiO_2–Na_2O, (c) SiO_2–(FeO + MgO); dark green and light green circles, high-Al and low-Al metapelite samples, respectively, from the Verbaard area (Rajesh *et al.*, 2018*b*); dark grey diamonds, metapelite inclusions within the Bulai pluton (Millonig *et al.*, 2008); blue diamond, metapelite sample TOV13 described by Perchuk *et al.* (2008*b*). (d) Chondrite-normalized REE spectrum of the studied metapelite in comparison with spectra of high-Al metapelites and low-Al metapelites (Boryta & Condie, 1990).

temperatures between 750 and 800 °C (area II in Fig. 13c). A dense convergence of isopleths in this *P*–*T* region (Fig. 13c) records the strong variations of mineral compositions in the shear bands. At these conditions the assemblage Grt + Crd + Bt + Pl + Qz + Sil + Rt still coexists with a melt of the following composition (wt%): SiO_2 67·7, Al_2O_3 14·3, FeO 0·7, MgO 0·3, CaO 0·6, Na_2O 4·4, K_2O 3·4, H_2O 8·6 (see red four-pointed star in Fig. 11a–d, normalized to water-free basis). However, the melt content at these conditions is below 5 vol% (Fig. 13d).

Conventional thermobarometry

Coexistence of Ti-bearing biotite with rutile and presence of graphite in the quartzofeldspathic domains of the rock LP19-11 justify an application of the Ti-in-biotite thermometer calibrated specifically for graphite-bearing peraluminous metapelites (Henry *et al.*, 2005). A clear negative correlation of the TiO_2 content of biotite with X_{Mg} for different generations of biotite in the rock (Fig. 6a) indicates that their compositions reflect primary conditions of biotite crystallization. Figure 14 distinguishes two groups of data points. The smaller group 1 includes individual biotite inclusions in garnet (Fig. 6a). Excluding two extreme data points, this group occupies the temperature interval at 820–830 °C. Some data points of biotite from the quartzofeldspathic domains and shear bands (Fig. 6a) also lie within this range. Nevertheless, dominant biotite data points define a larger group 2 covering the interval 800–820 °C (Fig. 14). Coincidence of the biotite data points from the quartzofeldspathic domains and shear bands indicates that despite different textural positions, these biotites crystallized during the same event in the rock evolution. Overall, the range 800–830 °C (Fig. 14) estimated using the Ti-in-biotite thermometer (Henry *et al.*, 2005) is in a good agreement with the results of the phase equilibria modeling (Fig. 13a–c).

Saturation of the rock system with TiO_2 (presence of rutile) also allows application of the thermometer based on the Ti solubility in garnet (Kawasaki & Motoyoshi, 2007). Profile C1–C2 (Fig. 7a) has been chosen to illustrate the applicability of this tool. The TiO_2 content along this profile varies unsystematically at a mean value of ~0·02 wt% (Fig. 15). Temperatures calculated using equations from Kawasaki & Motoyoshi (2007) vary within 780–880 °C with a mean value at 845 °C (Fig. 15). Taking into account the accuracy of the Ti-in-garnet method (Kawasaki & Motoyoshi, 2007), the mean value is consistent with the peak temperatures obtained from the phase equilibria modeling and the Ti-in-biotite thermometry (Henry *et al.*, 2005).

Evolution of the shear bands is reflected in variations of the composition of biotite and cordierite. Mg-numbers of these minerals systematically increase toward the contacts with garnet, reflecting

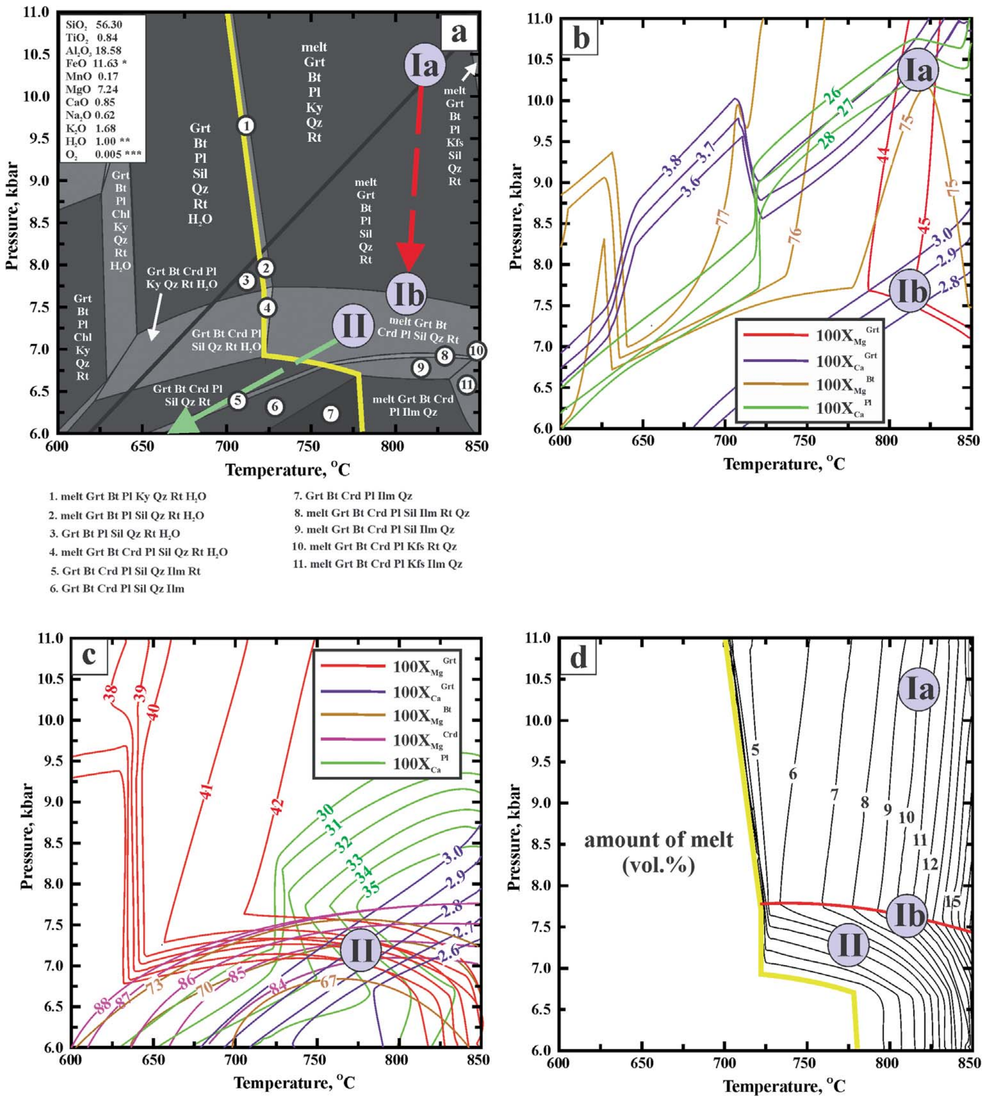

Fig. 13. Results of the phase equilibria modeling for the bulk composition of the metapelite sample LP19-11. (a) P–T pseudosection calculated for the bulk composition shown in the inset table (*, calculated from Fe_2O_3 measured with XRF; , estimated from the T–M_{H2O} and P–M_{H2O} pseudosection; *, arbitrary value); yellow line is solidus; Ia, peak P–T parameters [see (b)]; Ib, presumable P–T condition of formation of the low-Ca domains and channels in garnet (Fig. 6c); II, P–T parameters of the formation of the shear bands [see (c)]; red dashed arrow is a P–T path of sub-isothermal decompression of the rock; light green dashed line is extrapolation of the path from Fig. 16. (b) Isopleths corresponding to compositions of minerals at the peak P–T conditions (see text). (c) Isopleths corresponding to compositions of minerals in the shear bands (see text). (d) Isolines of amount of melt (vol%); yellow line is solidus [see (a)]; red line separates cordierite-free and cordierite-bearing portions of the diagram [see (a)].

late Fe–Mg exchange. Isopleths on the P–T pseudosection (Fig. 13c) show that the increase of X_{Mg} of both minerals proceeds via cooling. Nevertheless, local mineral re-equilibration during evolution of the shear bands could not be fully characterized by the pseudosection constructed for the bulk-rock composition, and, thus, conventional local mineral thermobarometry should be applied. We used the equilibrium (1) experimentally calibrated by Aranovich & Podlesskii (1989) and the composition of contacting garnet and cordierite to estimate P–T conditions during the late evolution of the shear bands. Pressure values calculated via equilibrium (1) are dependent on the water content in cordierite (or water content in the equilibrium fluid). Assuming saturation of cordierite with a $H_2O + CO_2$ fluid and using relations from Harley *et al*. (2002), the values 0·15–0·18 molecules of CO_2 per formula unit (p.f.u.) estimated using Raman spectra (Fig. S3, Supplementary Materials) correspond to $X_{CO2} = CO_2/(CO_2 + H_2O)$ of 0·22–0·25 in the cordierite. This CO_2 mole fraction in cordierite corresponds to $X_{CO2} \sim 0{\cdot}8$ ($X_{H2O} \sim 0{\cdot}2$) in the coexisting aqueous–carbonic fluid (Johannes & Schreyer, 1981). P–T values calculated via equilibrium (1) for $X_{H2O} = 0{\cdot}2$ in the fluid for seven garnet–cordierite contacting pairs define a P–T path from 650 °C/5·5 kbar to 550 °C/4·5–5·0 kbar (Fig. 16). Most data points are situated within the sillimanite stability field (Fig. 16) that is supported by the petrographic observations and Raman investigations of Al-silicates in the shear bands.

GEOCHRONOLOGY

Polished crystals of zircon, monazite and rutile were analyzed for the sample LP19-11 and TOV13 studied by Perchuk *et al*. (2008*b*)

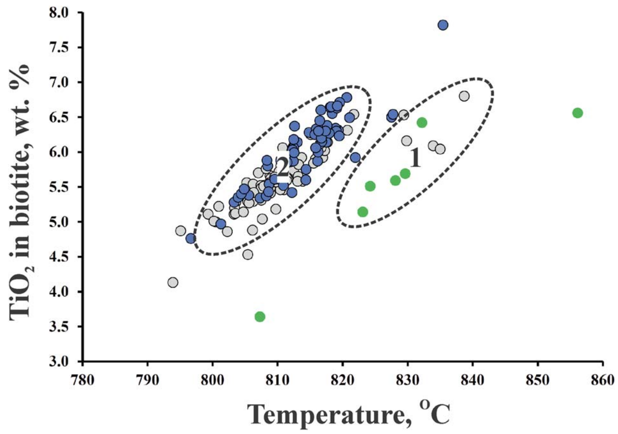

Fig. 14. Results of the temperature calculation using the Ti-in-biotite thermometer (Henry *et al*., 2005) vs the TiO_2 content in biotite. Markers – see Fig. 6. Two groups of data points considered in the text are outlined by dashed ovals.

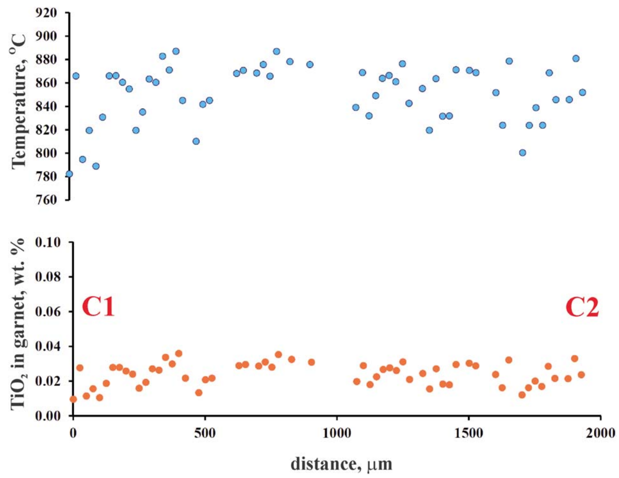

Fig. 15. Variations of the TiO_2 content in garnet along the profile C1–C2 (Fig. 7a) and temperatures calculated using the Ti-in-garnet tool (Kawasaki & Motoyoshi, 2007).

for comparison. Results are presented in Table S7 of Supplementary Materials.

Monazite

Thirteen analyses on 12 light yellow monazite fragments from sample LP19-11 show Th/U ratios between five and 13. They are ~2 % discordant and give a weighted average $^{207}Pb/^{206}Pb$ age of 2011 ± 3 Ma (95 % confidence, MSWD = 0·31). Eleven analyses on two large monazite fragments were done for sample TOV13. All analyses show Th/U ratios between eight and 70 and are between 1 and 4 % discordant. A weighted average $^{207}Pb/^{206}Pb$ age is 2011 ± 5 Ma (95 % confidence, MSWD = 0·66), which is consistent with the result for sample LP19-11.

Rutile

Seven analyses on different crystals of rutile 70–200 μm in size from sample LP19-11 vary between 10 % normally and reversely discordant, and define an upper intercept age of 1963 ± 24 Ma

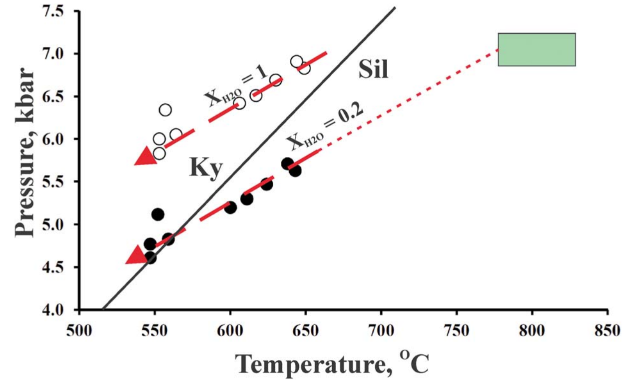

Fig. 16. *P–T* path calculated from the composition of contacting garnet and cordierite in the shear bands at $X_{H2O} = 0·2$ in an aqueous–carbonic fluid. Short-dashed line is an extrapolation of the path to higher pressures and temperatures. Green rectangle shows a range of *P–T* conditions estimated for the beginning of the formation of the shear bands using the phase equilibria approach (Fig. 13a and c). The *P–T* path calculated for $X_{H2O} = 1$ is given for comparison. The Ky = Sil reaction line is taken from Holdaway (1971).

(95 % confidence; MSWD = 0·04) and a lower intercept around zero. Fourteen analyses on the 15 crystals of rutile from sample TOV-13 define a concordia age of 1970 ± 12 Ma (2σ), albeit with an MSWD of four. It is indistinguishable from the weighted average $^{207}Pb/^{206}Pb$ age of 1966 ± 11 Ma, with an MSWD of 0·5.

Zircon

Zircon grains in samples LP19-11 and TOV13 are 40–100 μm in size and typically have an ovoid shape (Fig. 17). Core-to-rim structures can be discerned in some of them, but internal structures are diffuse in CL images. Many of them contain rounded cores of 20–30 μm across and rims of similar thickness, which can be distinguished by subtle difference in CL brightness (grain 18 in Fig. 17). Remnant oscillatory zoning is rarely visible in the core (grain 12 in Fig. 17). Inclusions of CL-bright crystals, probably apatite, and cracks are common in the rims.

Forty-nine analyses were done on 38 zircon grains from sample LP19-11. Most of the data fall close to the concordia, with no more than 30 %, but mostly less than 10 %, discordance. The $^{207}Pb/^{206}Pb$ ages range between 2000 and 3290 Ma, with a dominant cluster around 2000 Ma (Fig. 18a). Seventeen of these younger analyses define an upper intercept age of 2015 ± 2 Ma (MSWD 1·6; Fig. 18b), and a lower intercept around zero. The data points with ages older than *c.* 2 Ga cannot be interpreted as a discordia with a lower intercept age at *c.* 2 Ga, and, for instance, an upper intercept age close to the oldest zircon age at 3·3 Ga. Some of the data points lie below this discordia, and could be interpreted as reflecting zero-age Pb loss. A significant number of analyses lie above the discordia. Some are formally concordant with ages of 2·78, 2·38–2·30, 2·24 and 2·14–2·10 Ga.

Fifty-six analyses were done on 46 grains from sample TOV13. Three of them contained more than 0·5 % common Pb and were discarded. Four more analyses, with discordance levels between 16 and 85 %, and $^{207}Pb/^{206}Pb$ ages of 1·82–1·85 (n = 3) and 5 Ga (n = 1) were also disregarded. Of the remaining analyses, three have $^{207}Pb/^{206}Pb$ ages of 1985–1988 Ma, 24 show smoothly varying $^{207}Pb/^{206}Pb$ ages of 1994–2017 Ma, 15 have ages of 2017–2172 Ma, and the remaining seven have widely varying ages between 2286 and 2898 Ma. The 24

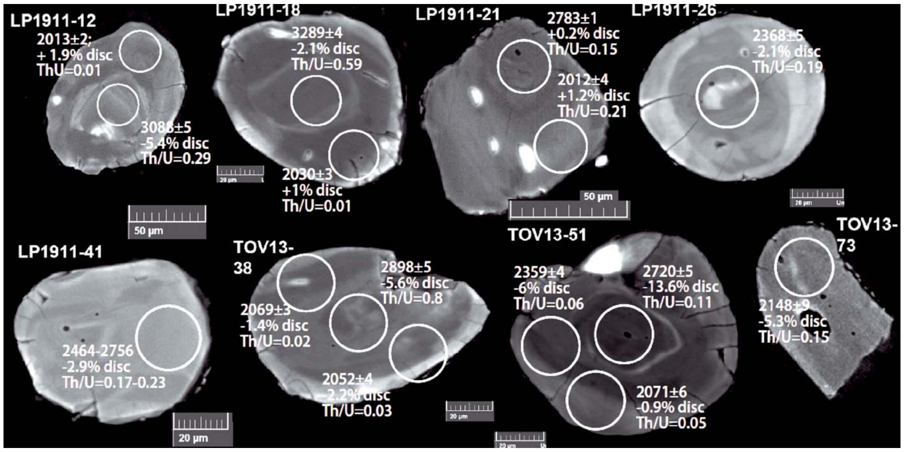

Fig. 17. CL images of some measured zircons from samples LP19-11 and TOV13.

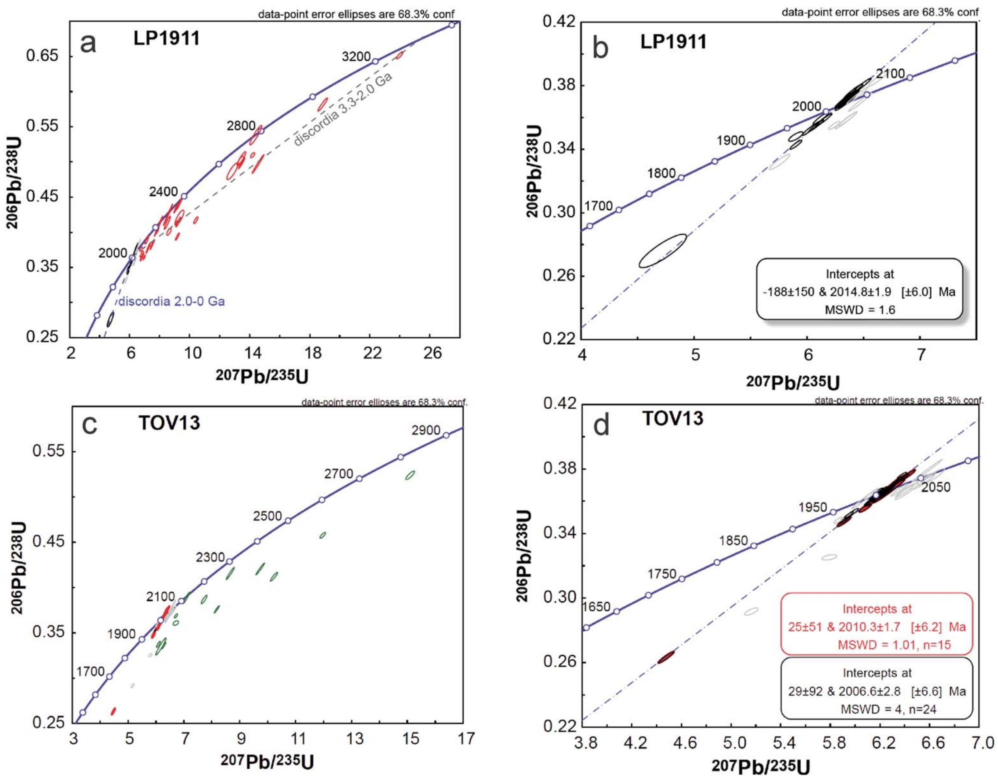

Fig. 18. U–Pb concordia plots for zircons from metapelites LP19-11 and TOV13. (a) All analyses for sample LP19-11. (b) Detail of (a) showing the discordia for 17 younger analyses defining an upper intercept age of 2015 ± 2 Ma. (c) All analyses for sample TOV13. (d) Detail of (c) showing the discordia for younger analyses.

analyses with $^{207}Pb/^{206}Pb$ ages of 1994–2017 Ma define a discordia with an upper intercept at 2007 ± 3 Ma, but with an MSWD of four (Fig. 18c). If only the 15 zircons are used with $^{207}Pb/^{206}Pb$ ages of 2004–2017 Ma, the discordia becomes statistically acceptable (MSWD = 1) with an upper intercept age of 2010 ± 2 Ma. The weighted average $^{207}Pb/^{206}Pb$ age of the group of 24 analyses is 2007 ± 2 Ma (one analysis rejected), but with an MSWD = 3. Of the older analyses, most of those with $^{207}Pb/^{206}Pb$ ages <2·13 Ga are concordant, but all those of 2·1–3·0 Ga are discordant (Fig. 18d).

There is a scattered correlation between Th/U ratio and the $^{207}Pb/^{206}Pb$ age for zircons from both samples (Fig. S5, Supplementary Materials). Analyses with $^{207}Pb/^{206}Pb$ ages above 2·42 Ga for zircons from LP19-11 show Th/U > 0·1. Younger analyses defining an upper intercept age of 2015 ± 2 Ma (Fig. 18b) have Th/U < 0·04. For sample TOV13, zircons with ages up to 2130 Ma have Th/U ratios below 0·1 (Fig. S5, Supplementary Materials). The older zircon grains have a tendency to have Th/U up to 0·8. The correlation between Th/U and age (Fig. S5, Supplementary Materials) combined with small size of zircon grains could mean that some of the obtained ages are mixed ones. This is supported by the fact that some ablation signals could be divided into the start and the end portions, which gave different ages (an example is a zircon crystal 41 in sample LP19-11; Fig. 17). The

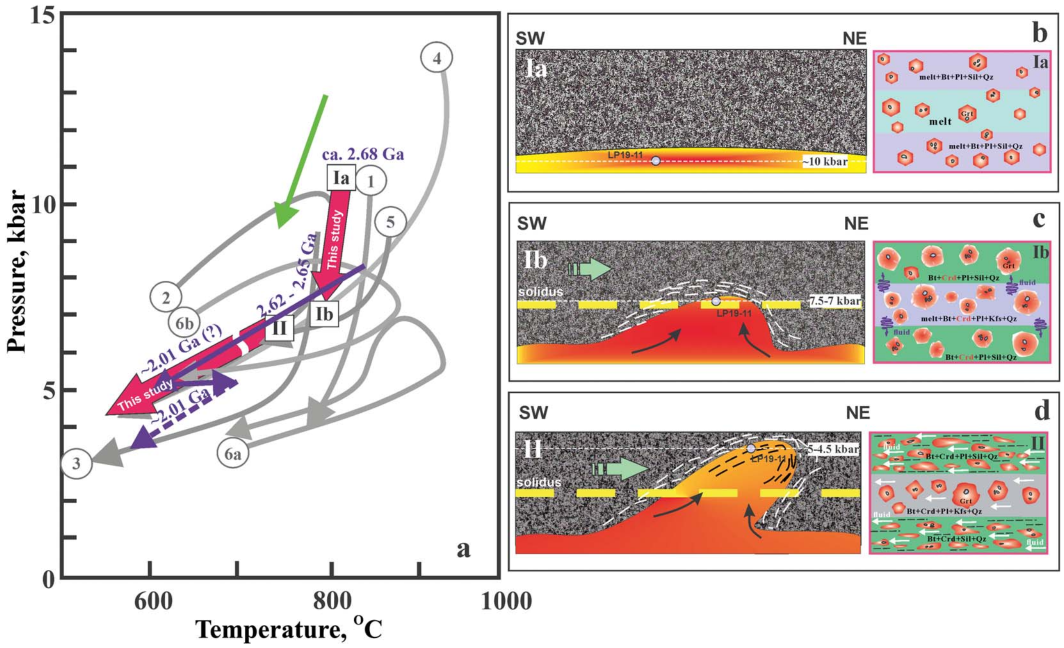

Fig. 19. Evolution of the metapelite LP19-11 from the Ha-Tshnazi closed structure during exhumation. (a) Kinked *P–T* path (red arrows) derived for the metapelite (stages Ia, Ib, and II; see Fig. 13a-c). Published *P–T* paths for metapelitic rocks from the CZ (grey arrows): 1, Droop (1989); 2, Zeh *et al*. (2004); 3, Tsunogae & Miyano (1989); 4, Tsunogae & van Reenen (2006); 5, Millonig *et al*., 2008; 6a and 6b, Brandt *et al*. (2018) (a, for the Neoarchean event; b, for the Paleoproterozoic event). Blue continuous arrows show the decompression cooling and isobaric heating portions of the *P–T* path for the Neoarchean event deduced by Perchuk *et al*. (2008*a*, 2008*b*) for metapelite TOV13 from the Ha-Tshanzi structure; dashed blue arrow is the decompression cooling path for the Paleoproterozoic event deduced from rocks from discrete shear zones that overprint cross folds (Perchuk *et al*., 2008*a*, 2008*b*). Green arrow shows the decompression cooling *P–T* path for the garnet-bearing Singelele granites (Rajesh *et al*., 2018*a*). (b–d) Schematic illustrations showing stages of the exhumation of the Ha-Tshanzi structure and their effects on the metapelite. (b) Partial melting at 810–830 °C and ~10 kbar within the metapelite sequence (yellow to red in left figure) results in garnet growth in the rock and the onset of the melt segregation into proto-leucosome (blue stripe in right figure); melt inclusions (small blue spots in the garnet markers in right figure) are trapped in garnet grains. (c) Sub-isothermal [see (a)] diapiric rise of the partially molten material is influenced by the overall NE exhumation of the CZ (light green dashed arrow in left figure) resulting in an inclination of the diapir. As the diapir crosses the solidus (thick dashed yellow line in left figure) at 7·5–7 kbar, the leucosome (magenta stripe in right figure) crystallizes, reaction of the residual melt with biotite and garnet produces cordierite (Fig. 4d); fluid release (winding blue arrows in right figure) from the leucosome triggers cordierite growth in the melanosome layers (green stripes in right figure); low-Ca channels (pale dashes in the garnet markers in right figure) form at the edges of garnet grains. (d) Further exhumation proceeds along the decompression-cooling path (a) via solid-state shearing within the diapir (black and white dashed lines in left figure). Shearing in the melanocratic layers (green stripes in right figure) with participation of fluids (white straight arrows in right figure) results in attenuated garnets, whereas garnets in the solidified leucosome remain undeformed. The exhumation, presumably, restarted during the Paleoproterozoic event (*c*. 2·0 Ga) with reactivation of former shear zones (a, c).

correlation between age and the Th/U ratio in the interval of near-concordant ages 2·02–2·78 Ga (Fig. S5, Supplementary Materials) suggests that it could simply reflect analysis of mixed domains in zircon grains.

DISCUSSION

P–T path of the metapelite from the Ha-Tshanzi structure

Phase equilibria modeling reconstructed three principal points on the *P–T* path of the rock LP19-11 within the Ha-Tshanzi closed structure (Ia, Ib, and II in Figs 13a–d and 19a–c). Stage Ia corresponds to partial melting within the metaplite sequence at 810–830 °C and ~10 kbar (Fig. 19a and b). The interval (Ia)–(Ib) represents the sub-isothermal stage of exhumation from the metamorphic peak to pressures of ~7·5 kbar (Figs 13a, b and 19a, c). The *P–T* path from (Ia) to (Ib) is vividly documented by the garnet composition isopleths in Fig. 13b. The path proceeds subparallel to the subvertical $X_{Mg}{}^{Grt}$ isopleths 0·44 and 0·45, reproducing nearly constant $X_{Mg}{}^{Grt}$ of garnet that is unmodified by the interaction with the later shear bands (profile C1–C2 in Fig. 7). In contrast, $X_{Ca}{}^{Grt}$ appreciably drops along this path in accordance with the nearly symmetric zoning of garnet porphyroblasts with respect to X_{Ca} (Fig. 8) that formed before the development of the zoning with respect to X_{Mg}. Both Ti-in-mineral tools also indicate sub-isothermal conditions of mineral equilibria in metapelite LP19-11 (Figs 14 and 15).

The termination of the sub-isothermal decompression path (Ib) (Figs 13a, b and 19a, c) is recorded by the composition of low-Ca domains and near-radial channels at the edges of garnet grains (Fig. 7c). Values of X_{Ca} in these microstructures are overall lower than these values in the garnet zones, which they cross. This reflects further decrease of the Ca content in correspondence to the X_{Ca} isopleths (Fig. 13b and c). The channels look very similar to so-called stringers; that is, radially oriented linear zones emanating from the rim of garnet and directed toward the core (e.g. Perchuk & Philippot, 2000). The stringers are suggested to form through healing of microscopic cracks in garnet at an early stage of rim growth in the presence of fluids (e.g. Perchuk & Philippot, 2000), probably via a replacement process involving dissolution at the tip of an advancing crack and re-precipitation of new garnet (e.g. Prior, 1993; Whitney, 1996). They often contain mineral inclusions indicative of the conditions of their formation. In the case of metapelite LP19-11, the low-Ca domains and near-radial channels in garnet locally contain inclusions of sillimanite and quartz (Fig. 7c). The absence of cordierite inclusions suggests that the low-Ca domains and near-radial channels in garnet were formed beyond the cordierite stability field. In fact, *P–T* conditions estimated for the formation of these structures are located between the Crd-free and Crd-bearing phase fields in the pseudosection (area Ib in Fig. 13a). Appearance of the low-Ca stringers along the garnet edges in contact with the undeformed quartzofeldspathic matrix (Fig. 7c) indicates that the stringers formed prior to the shear bands in the rock (Fig. 19c).

Records of the equilibrium with a melt during the metamorphic peak and uplift

Phase equilibria modeling predicts 9–11 vol% of melt coexisting with the rock at the peak conditions 810–830 °C and 10–10·2 kbar (Fig. 13d). The modeled melt fraction is higher than a threshold of ~7 vol% that is sufficient to create an interconnected system of melt films in the partially molten felsic protolith (e.g. Rosenberg & Handy, 2005), but is not enough for further melt segregation (e.g. Brown *et al*., 1995; Brown & Solar, 1998). Nevertheless, the presence of a leucosome in sample LP19-11 (Fig. 3a and b), which is clear evidence for melt segregation, suggests that the amount of melt during the metamorphic peak and uplift was higher than the modeled values. The major element composition of the sample (Figs. 12a–c) is comparable with that of high-Al metapelites of the CZ (Boryta & Condie, 1990; Rajesh *et al*., 2018*b*), whereas the REE pattern (Fig. 12d) resembles that of low-Al metapelites. If the difference between these types of metapelites is related to different proportions of the preserved melt (e.g. Rajesh *et al*., 2018*b*), the metapelite LP19-12 can be interpreted as the garnet-rich restite that experienced significant melt extraction.

Isolines of the amount of melt (Fig. 13d) indicate that the melt fraction increased by 1–2 vol% during the sub-isothermal decompression down to a pressure of ~7·5 kbar. Such an increase of the melt fraction is typical for dehydration melting reactions in a rock during a pressure drop (Le Breton & Thompson, 1988; Vielzeuf & Holloway, 1988). Former melt polyphase inclusions in cores of garnet grains (Fig. 5a–d) provide convincing evidence for these reactions both at the metamorphic peak and during the sub-isothermal decompression of the rock. Analyses of the inclusions show SiO_2, Al_2O_3, and CaO contents comparable with the compositions of the melts predicted by PERPLE_X and melts produced in the experiments on melting of peraluminous metapelites at pressure above 7 kbar (Le Breton & Thompson, 1988; Vielzeuf & Holloway, 1988; Carrington & Harley, 1995; Koester *et al*., 2002) (Fig. 11b and c). Higher MgO + FeO content and lower $K_2O + Na_2O$ content of the inclusions indicate their late modification (e.g. Cesare *et al*., 2015), first of all by dissolution of host garnet in the melt inclusions during decompression (e.g. Hiroi *et al*., 2014). The small size of the inclusions and much larger volume of host garnet also creates favorable conditions for extensive retrograde exchange (Cesare *et al*., 2015). High bulk MgO/FeO ratio in the cryptocrystalline inclusions and elevated X_{Mg} in biotite in the crystallized inclusions (Fig. 6a–c) resulted from Fe redistribution into the host garnet (Hiroi *et al*., 2014; Cesare *et al*., 2015), which is expressed in local X_{Mg} minima in profiles at the contacts with the inclusions (Fig. 8).

The notable zoning of garnet with respect to phosphorus (Figs 7d and 8) is another line of evidence for the rock evolution in the presence of a melt. Apatite inclusions in the P-poor garnet core (Fig. 7d) suggest that the garnet coexisted with a small fraction of peraluminous melt, which was initially (over)saturated with phosphorus (e.g. London *et al*., 1999; Yakymchuk, 2017; Yakymchuk & Acosta-Vigil, 2019) and buffered the P content of garnet to low values. Saturation of the melt in phosphorus is supported by relatively high content of P_2O_5 (up to 0·4 wt%) in the measured areas of the melt inclusion, which do not show visible apatite grains. A core-to-rim increase of the P concentration (Fig. 8) correlated with the distribution of phosphate inclusions in garnet (Fig. 7d) documents an increase of the degree of partial melting via phosphate-consuming reactions (Hiroi *et al*., 1997; Yang & Rivers, 2002; Kawakami & Motoyoshi, 2004; Kawakami & Hokada, 2010; Kobayashi *et al*., 2011). Rare monazite inclusions in garnet cores suggest incongruent dissolution of REE-bearing apatite in the melt during the prograde melting (Yakymchuk, 2017; Yakymchuk & Acosta-Vigil, 2019). Absence of apatite in the phosphorus-richer shells S1 and S2 (Fig. 7d) indicates undersaturation of the melt with phosphorus, which could correspond to an increase of the melt volume in the system (e.g. London *et al*., 1999; Yakymchuk, 2017; Yakymchuk & Acosta-Vigil, 2019), which occurred during decompression (Fig. 13d). In fact, the start of the increase of the phosphorus content in the garnet roughly coincides with the beginning of the decrease in the Ca content in this mineral (Fig. 8), which reflects decompression (Fig. 12b and c). Formation of the phosphorus-depleted outer zone (OZ in Fig. 7d) corresponds to a final crystallization of the melt at the end of the isothermal decompression path (Ia)–(Ib). The uneven interface between the OZ and S2 zones (Fig. 7d) implies resorption of the garnet, which occurred in the field melt + Grt + Bt + Crd + Pl + Sil + Qz (Fig. 13a). Crystallization of feldspars, which are good containers of phosphorus (e.g. Bea *et al*., 1994; London *et al*., 1999; see Fig. 7d), and, probably, additional crystallization of phosphates resulted in a drop of the phosphorus content in the garnet. Massive crystallization of feldspars (and quartz) led to accumulation of Cr and Sc in the residual melt, resulting in enrichment of the outer zones of garnet in these elements (Fig. 8), which were formed along with Cr-bearing sillimanite and the later generations of biotite, which are Cr-rich, as well (Fig. 6b). This conclusion is consistent with partitioning of Cr and Sc between metapelite minerals and granitic melt (e.g. Bea *et al*., 1994).

Thus, regular garnet zoning with respect to measured trace elements indicates not only an equilibrium of the garnet with the melt along the sub-isothermal decompression stage (Ia)–(Ib) (Fig. 19a), but also implies an almost total solidification of the melt by the end of this stage (Fig. 19c). The assemblage of the lower-X_{Ca} peripheral zones of garnet with small inclusions of sillimanite (Fig. 4a–c), as well as biotite, K-feldspar and quartz in the leucosome of the metapelite sample LP19-11 characterizes the stage of melt crystallization before the shear deformation event. This assemblage allows estimation of the water activity (a_{H2O}) from the equilibrium

$$\mathrm{Phl(Ann) + Sil + 2Qz = Prp(Alm) + Kfs + H_2O.} \qquad (2)$$

Using the winTWQ (version 2.32) software (Berman, 2007), involving self-consistent end-member mineral properties according to Berman (1988) and solid solution models from Berman & Aranovich (1996), values of water activity ~0·1 were obtained. Low water activity in the fluid is also responsible for the reaction rims of $H_2O–CO_2$-bearing cordierite in the assemblage with K-feldspar and sillimanite around biotite flakes in the quartzofeldspathic domains (Fig. 4d). Calculations via the equilibrium

$$\frac{1}{3}\text{Phl}\left(\text{Ann}\right)+\text{Sil}+\frac{3}{2}\text{Qz}=\frac{1}{2}\text{Crd}\left(\text{Fe}-\text{Crd}\right)+\frac{1}{3}\text{Kfs}+\frac{1}{3}\text{H}_2\text{O} \quad (3)$$

support the above low water activity, which was established in the fluid during solidification of the water-undersaturated CO_2-bearing granitic melt. Evidence for the presence of CO_2 in the melt is graphite developed in the coarse-grained quartzofeldspathic domains of the rock. K-feldspar rims on plagioclase in these domains (Fig. 4a–c) are representation of Korzhinskii's reaction controlled by K and Na activities in a fluid related to salt components (e.g. Aranovich & Safonov, 2018). Thus, low activity of H_2O was related both to the presence of CO_2 and alkali salt components in the residual fluid (e.g. Aranovich & Newton, 1997).

Transition from a melt-controlled to shear-controlled regime of exhumation

After partial extraction of the melt and solidification of the remaining melt at the end of the near-isothermal decompression stage, further exhumation was accompanied by solid-state ductile deformation (Fig. 19d). This is expressed in the formation of the cordierite-bearing shear bands in the metapelite LP19-11 (Fig. 3a–c). It is logical to suggest that further decompression followed immediately after the sub-isothermal decompression stage at 810–830 °C and was related to a deceleration of the exhumation because of a change in the rock rheology. Magmatic diapirs are able to continue rising after magma crystallization, and the solid-state rise of diapirs may cause the superimposition of various generations of foliation inside both diapir and surrounding rocks (e.g. Weinberg & Podladchikov, 1995; Fig. 19d). In the case of the metapelite LP19-11, the shear bands are parallel to the earlier foliation defined by leucosomes (Fig. 3a and b), suggesting that solid-state deformation continued earlier deformations during the melt-mediated exhumation in the same direction and occurred at the same tectono-thermal event.

In contrast to the earlier isothermal decompression stage mediated by melt, solid-state exhumation was accompanied by significant cooling expressed by an Fe–Mg exchange of garnet with biotite and cordierite and formation of the garnet zoning with respect to X_{Mg} at the contacts with these minerals (Figs 7b, 8, 9b and 10c). *P–T* values calculated using the equilibrium (1) form a linear *P–T* path with a slope of ~75 °C $kbar^{-1}$ starting from a temperature of ~650 °C at a pressure of ~5·5 kbar to a temperature of ~550 °C at a pressure of ~4·5 kbar (Fig. 16). An extrapolation of the *P–T* path (Fig. 16) to higher *P* and *T* proceeds directly to the *P–T* region estimated from the phase equilibria modeling for the beginning of the formation of the shear bands (area II in Fig. 13a and c). The *P–T* path in Fig. 16 and its extrapolation coincides with the *P–T* path derived by Perchuk *et al*. (2008*b*) for the metapelite TOV13 from the Ha-Tshanzi structure (Fig. 19a).

Formation of the shear bands destroyed the earlier zoning of garnet with respect to trace elements with formation of new P-bearing (apatite) and Cr-bearing (sillimanite, biotite) phases. Biotite in the shear bands is the Cr-richest generation of this mineral in the rock (Fig. 6b) because of formation at the expense of Cr-rich peripheral zones of the garnet porphyroblasts. Abundance of biotite and H_2O–CO_2-bearing cordierite in the shear bands demonstrates that they were forming with the participation of fluids. Absence of K-feldspar in the shear bands results in a strong displacement of equilibria (2) and (3) to the left, probably because of relatively high water activity. Because K-feldspar is absent, water activity cannot be estimated directly for the shear bands. Nevertheless, CO_2 activity (a_{CO2}) can be estimated from the CO_2 content in cordierite using the equation of Harley *et al*. (2002). The values 0·15–0·18 of CO_2 molecules p.f.u. of cordierite correspond to a_{CO2} of 0·6–0·7. Considering the equation of state for the H_2O–CO_2 fluid from Kerrick & Jacobs (1981), this a_{CO2} would correspond to a_{H2O} ~ 0·5–0·4, which is higher than the water activity during crystallization of the leucosome at the end of the sub-isothermal decompression stage (Ib). Difference in water activity probably reflects different sources of fluids; that is, an internal source (crystallizing melt in the leucosome) at the end of the sub-isothermal decompression stage (Ib) and an external source during the formation of the shear bands at the onset of the decompression cooling stage (II) (Fig. 19a and d).

Interpretation of the Ha-Tshanzi structure as a gneiss dome driven by granite diapirism

The closed structures in the Central Zone (CZ) of the Limpopo Complex randomly distributed throughout the Central Zone (Fig. 1b) were initially interpreted as large Neoarchean sheath folds (e.g. Roering *et al*., 1992; van Kal, 2004) or as results of superimposed folding during the Paleoproterozoic (Watkeys, 1979; Fripp, 1983; Holzer *et al*., 1998). However, these structures are commonly unrelated to any shear-zone system and are enclosed in granoblastic granulites that were intensely deformed (isoclinal folds with near-vertical foliation) during the early regional deformational event at 2·72–2·65 Ga. These observations argue against the interpretation of the closed structures as sheath folds.

The Ha-Tshanzi closed structure bears structural and petrological features that are characteristic for gneiss domes driven by granitic diapirism (e.g. Whitney *et al*., 2004). It is near-ellipsoidal in shape, involves the Singelele-type leucocratic anatectic granitoids and metapelitic diatexites, and contains disrupted layers of supracrustal host rocks of the Beit Bridge and Mussina complexes (Fig. 2a). *P–T* data for the metapelite LP19-11 show that the structure was exhumed by 15–17 km (5–5·5 kbar), with initial sub-isothermal exhumation within the first 7–9 km that was mediated by granitic melts (Fig. 19a and c). These petrological features are hardly characterisrtic for sheath folds and superimposed folds.

An overall predominance of supracrustal quartzites, calc-silicate rocks and marbles of the Beit Bridge Complex and ultramafic lithologies of the Mussina suite over granitoids in the core (Fig. 2a) and a deviation of the Ha-Tshanzi structure from the vertical position (40–45°; Fig. 2b and c; Fig. S1 in Supplementary Materials) would suggest against an interpretation of the Ha-Tshanzi closed structure as a diapir-related gneissic dome. However, the outcrop of granitic cores and surrounding (mantling) rocks in the gneissic domes is dependent on the level of exposure related to the denudation processes, so that distinct granitic cores are not always well exposed (e.g. Whitney *et al*., 2004). This seems to be the case for the Ha-Tshanzi dome. Smit *et al*. (2011) deduced that the eastern areas of the CZ (where the Ha-Tshanzi structure is located; Fig. 1a) represented a deeper level of the crust in comparison with the western areas, where similar closed structures expose distinct granitic cores (i.e. the Avoca closed structure; Boshoff *et al*., 2006; Perchuk *et al*., 2008*a*, 2008*b*; van Reenen *et al*., 2008, 2019; Smit *et al*., 2011). Whitney *et al*. (2004) noted that the diapiric doming may be greatly influenced by the balance between the vertical and lateral crustal flows in the orogenic belts, and a predominance of lateral flow would modify the inclination of the gneissic dome toward a recumbent position. This explains the inclination at 40–45° of the Ha-Tshanzi closed structure (and other closed structures in the CZ), which records the overall NE-directed exhumation of the complex prior to emplacement of the Bulai pluton at 2·61–2·58 Ga (Fig. 19c and d; Perchuk *et al*., 2008*a*, 2008*b*; van Reenen *et al*., 2008, 2019; Smit *et al*., 2011).

Timing of the formation of the Ha-Tshanzi granite–gneiss dome

The studied metapelite samples from the Ha-Tshanzi dome contain abundant data indicating an effect of the Paleoproterozoic overprint at *c*. 2·01 Ga (Fig. 18b and d). They include data on zircon grains with Th/U < 0·1, as well as on monazite with exactly the same age. The weighted ages for rutile from LP19-11 (1963 ± 24 Ma) and TOV13 (1966 ± 11 Ma) are indistinguishable from the mean age 1967 ± 2 Ma reported by Brandt *et al*. (2018) and Kröner *et al*. (2018) for rutile from metapelites at the western margin of the Bulai pluton and reflect further cooling.

However, three sources of data show that the Ha-Tshanzi granite–gneiss dome formed, or at least began to form, prior 2·61 Ga; that is, before the intrusion of the Bulai pluton. First, structural geometry of the Ha-Tshanzi gneiss dome is identical to that of the Avoca closed structure in the western area of the CZ (Fig. 1b). Formation of this was accurately dated at 2·63–2·62 Ga (Boshoff *et al*., 2006; van Reenen *et al*., 2008, 2019). Second, the near-isothermal decompression evolution in the beginning of the retrograde *P*–*T* path deduced for metapelites from the Ha-Tshanzi structure (Fig. 19) is in accordance with previous studies (Droop, 1989; Tsunogae & Miyano, 1989; Zeh *et al*., 2004; Tsunogae & van Reenen, 2006; Millonig *et al*., 2008; Rajesh *et al*., 2018*b*; see compilation in Fig. 19). Millonig *et al*. (2008) dated the sub-isothermal decompression stage at 2644 ± 8 Ma by applying metamorphic and age data obtained from true metapelitic, charnoenderbitic and enderbitic xenoliths trapped within the Bulai pluton. Thus, sub-isothermal decompression was characteristic for the entire CZ before the emplacement of the Bulai granites at 2·61–2·58 Ga. The best candidate for granitic magmas that actively mediated the exhumation of the Ha-Tshanzi structure is the Singelele leucocratic granites. They were voluminously emplaced throughout the CZ within the period 2·68–2·62 Ga (e.g. Kröner *et al*., 1999, 2018; Smit *et al*., 2011; Rajesh *et al*., 2018*a*; van Reenen *et al*., 2019). Phase equilibria modeling of the garnet-bearing varieties of the Singelele granites showed that they started their crystallization at pressures above 10 kbar followed by sub-isothermal decompression (Rajesh *et al*., 2018*a*; Fig. 19). The close association of the Ha-Tshanzi metapelites with the Singelele granites (Fig. 2a) and their close *P*–*T* evolution is evidence that the exhumation of the Ha-Tshanzi dome occurred prior to 2·61 Ga.

However, the Neoarchean metamorphism is not recorded in the accessory minerals of the studied samples LP19-11 and TOV13 from the Ha-Tshanzi dome. Data on zircons with ages older than 2·01 Ga are scattered over a wide age interval (Fig. S5, Supplementary Materials), making interpretation on their provenance highly problematic. This situation with the geochronological data from the Ha-Tshanzi structure is not unique for the CZ. Numerous geochronological studies of metapelites outside the Bulai pluton emphasized that any record on the Neoarchean metamorphic event is extremely rare in these rocks (Kröner *et al*., 1998; Boshoff *et al*., 2006; van Reenen *et al*., 2008; Kramers & Mouri, 2011). Evidence for this event is detectable predominantly in xenoliths in the Bulai pluton (e.g. Millonig *et al*., 2008; Kröner *et al*., 2018). In turn, rocks outside the pluton demonstrate the overwhelming effect of the overprint at 2·01–2·02 Ga as zircon overgrowths, newly formed monazite and rutile grains (Jaeckel *et al*., 1997; Kröner *et al*., 1998, 2018; van Reenen *et al*., 2008; Kramers & Mouri, 2011). The Paleoproterozoic event at *c*. 2·01 Ga is explained as a high-grade regional thermal and fluid overprint (van Reenen *et al*., 2008, 2019; Boshoff *et al*., 2006; Perchuk *et al*., 2008*a*, 2008*b*; Kramers & Mouri, 2011; Smit *et al*., 2011; Rajesh *et al*., 2018*a*), associated, probably, with the influence of the Bushveld LIP magmatism at *c*. 2·05 Ga (e.g. Millonig *et al*., 2010; Smit *et al*., 2011; Rajesh *et al*., 2020). The Paleoproterozoic event produced no major fold deformation (Jaeckel *et al*., 1997; Kröner *et al*., 1998, 2018; van Reenen *et al*., 2008, 2019; Smit *et al*., 2011), whereas shear deformation was manifested by discrete centimeter to meters wide north–south-trending shear zones, as well as by reactivation of Neoarchean shear structures (e.g. Smit *et al*., 2011). The Tshipise Straightening Zone, which bounds the CZ in the south (Fig. 1a and b; Horrocks, 1983), was reactivated as a strike-slip shear zone during this event. Narrow shear zones were superimposed onto the north–south-trending 'cross-fold' structures (e.g. Smit *et al*., 2011) as well as onto the Bulai granites (e.g. Holzer *et al*., 1998). As for the Ha-Tshanzi dome specifically, the Paleoproterozoic event overprinted its earlier structures by discrete north–south-trending shear zones (e.g. Holzer *et al*., 1998; van Kal, 2004), and resulted in formation of a narrow zone of shear deformations immediately adjacent to the Bulai pluton (Fig. 2a) (Holzer *et al*., 1998).

The cooling with further decompression accompanied by shearing followed immediately after the sub-isothermal decompression stage and, thus, probably occurred during the Neoarchean event, rather than 'waiting' ~600 Myr. However, it cannot be excluded that the shear bands in the metapelite, being incipient during the Neoarchean exhumation, were reactivated and served as conduits for the massive influx of external fluids in the course of cooling during the Paleoproterozoic thermal event. Kramers & Mouri (2011) concluded that the resetting of Neoarchean ages during the Paleoproterozoic event in the CZ is related to mostly fluid influx at *c*. 2·01 Ga rather than thermal heating. Brandt *et al*. (2018) and Kröner *et al*. (2018) specifically noted that zircon recrystallization in metapelites during the Paleoproterozoic overprint was facilitated by a fluid. Rajesh *et al*. (2018*a*) provided evidence that the Singelele leucogranite was also affected by a metasomatic overprint at *c*. 2·0 Ga recorded both in the zircon overgrowths and in $^{40}Ar/^{39}Ar$ ages for halogen-bearing amphibole and biotite. Higher water activity recorded in the shear bands of the metapelite LP19-11 prove the influx of external fluids. Experimental studies show that fluids, especially salt-bearing, can serve as much stronger modifiers of zircon than melts (Geisler *et al*., 2007; Harlov & Dunkley, 2010). If so, the regression of temperatures between 650 and 550 °C recorded by Fe–Mg exchange reactions in the shear bands (Fig. 16) within the period between about 2010 Ma obtained from zircon and monazite and the age of about 1960 Ma obtained from rutile yields a cooling rate during the Paleoproterozoic event of ~2 °C Ma^{-1}.

CONCLUSION

Detailed study of a metapelitic granulite from the Ha-Tshanzi closed structure in the Central Zone of the Limpopo Complex provides petrological evidence in support of the interpretation of this structure as a diapir-related granite–gneiss dome developed within the period of time 2·68–2·62 Ga. Former-melt inclusions in garnet, regular garnet zoning with respect to Ca and trace elements (P, Cr, Sc), and phase equilibria modeling record the evolution of the mineral assemblage of the metapelite in the presence of a granitic melt. It was accompanied by sub-isothermal decompression at 810–830 °C from a pressure of 10–10·2 kbar down to 7–7·5 kbar (Fig. 19a–c). These data probably indicate the gravity-driven exhumation of melt-saturated migmatitic material within a granite–gneiss dome during the Neoarchean Limpopo orogeny prior to 2·61 Ga (Fig. 19b).

During decompression, the melt was partially extracted, separated from the garnet-rich restite and crystallized at pressures of ~7 kbar because of sequestering of water by cordierite, which formed in the assemblage at the end of the sub-isothermal decompression stage (Fig. 19a and c). These processes changed the rheology of the rocks and led to a transition from melt-dominated deformation to solid-dominated ductile shear deformation (Fig. 19c). The transition between different styles of deformation resulted in a deceleration of the exhumation and prevalence of cooling. The gentler slope of ~75 °C $kbar^{-1}$ of the decompression-cooling path marks a lower rate of exhumation within the depth interval 20–13 km. The Neoarchean evolution of the metapelite was strongly overprinted by the high-temperature Paleoproterozoic event at *c*. 2·01 Ga, during which reactivation of earlier shear zones, including shear bands in sample LP19-11, were mediated by aqueous–carbonic salt-bearing fluids.

Despite suggestion of the model for the diapir-related origin of the closed structures in the Central Zone of the Limpopo Complex, previous studies (Perchuk *et al*., 2008*a*, 2008*b*; Smit *et al*., 2011; van Reenen *et al*., 2019) failed to show persuasive evidence for either sub-isothermal decompression or active mediation of the exhumation by melts for these structures. Because all the closed structures in the Central Zone are structurally similar, the present study on the Ha-Tshanzi structure encourages revision of petrological data on other closed structures to unify this model.

FUNDING

This research is supported by the Russian Scientific Foundation (project 18-17-00206 to O.G.S., V.O.Y. and A.L.P.) and fulfilled under the Research Program (FMUF-2022-0004; 1021051302305-5-1.5.2;1.5.4) of the Korzhinskii Institute of Experimental Mineralogy RAS. The microprobe and Raman analytical work is supported by the Developing Program of the Moscow State University. D.D.v.R. and C.A.S. acknowledge support from the National Science Foundation of South Africa (project GUN: 81040) and from DST-NRF CIMERA at the University of Johannesburg through its director Professor Nicola Wagner.

SUPPLEMENTARY DATA

Supplementary data are available at *Journal of Petrology* online.

ACKNOWLEDGEMENTS

The authors thank Jiří Žák (Charles University, Prague), Johannes Wiest (University of Bergen) and an anonymous reviewer for constructive reviews.

REFERENCES

Aranovich, L. Y. & Newton, R. C. (1997). H_2O activity in concentrated KCl and KCl–NaCl solutions at high temperatures and pressures measured by the brucite–periclase equilibrium. *Contributions to Mineralogy and Petrology* **127**, 261–271.

Aranovich, L. Y. & Podlesskii, K. K. (1989). Geothermobarometry of high-grade metapelites: simultaneously operating reactions. In: Daly, J. S., Cliff, R. A. & Yardley, B. W. D. (eds) *Evolution of Metamorphic Belts*. *Geological Society, London, Special Publications* **43**, 45–61.

Aranovich, L. Y. & Safonov, O. G. (2018) Halogens in high-grade metamorphism. In: Harlov, D. E. & Aranovich, L. Y. (eds) *The Role of Halogens in Terrestrial and Extraterrestrial Geochemical Processes*. Cham: Springer, pp. 713–757.

Axelsson, E., Pape, J., Berndt, J., Corfu, F., Mezger, K. & Raith, M. M. (2018). Rutile R632–A new natural reference material for U-Pb and Zr determination. *Geostandards and Geoanalytical Research* **42**, 319–338.

Bartoli, O. & Cesare, B. (2020). Nanorocks: a 10-year-old story. *Rendiconti Lincei, Scienze Fisiche e Naturali* **31**, 249–257.

Bartoli, O., Acosta-Vigil, A., Ferrero, S. & Cesare, B. (2016). Granitoid magmas preserved as melt inclusions in high-grade metamorphic rocks. *American Mineralogist* **101**, 1543–1559.

Bea, F., Pereira, M. D. & Stroh, A. (1994). Mineral/leucosome trace-element partitioning in a peraluminous migmatite (a laser ablation-ICP-MS study). *Chemical Geology* **117**, 291–312.

Berman, R. G. (1988). Internally-consistent thermodynamic data for minerals in the system Na_2O–K_2O–CaO–MgO–FeO–Fe_2O_3–Al_2O_3–SiO_2–TiO_2–H_2O–CO_2. *Journal of Petrology* **29**, 445–522.

Berman, R. G. (2007). WinTWQ (version 2.3): a software package for performing internally-consistent thermobarometric calculations. *Geological Survey of Canada Open File* **5462**, 41.

Berman, R. G. & Aranovich, L. Y. (1996). Optimized standard state and solution properties of minerals I. Model calibration for olivine, orthopyroxene, cordierite, garnet, and ilmenite in the system FeO–MgO–CaO–Al_2O_3–TiO_2–SiO_2. *Contributions to Mineralogy and Petrology* **126**, 1–24.

Bingen, B., Davis, W. J., Hamilton, M. A., Engvik, A. K., Stein, H. J., Skar, O. & Nordgulen, O. (2008). Geochronology of high-grade metamorphism in the Sveconorwegian belt, S. Norway: U–Pb, Th–Pb and Re–Os data. *Norwegian Journal of Geology* **88**, 13–42.

Boryta, M. D. & Condie, K. C. (1990). Geochemistry and origin of the Archean Beit Bridge Complex, Limpopo Belt, South Africa. *Journal of the Geological Society, London* **147**, 229–239.

Boshoff, R., van Reenen, D. D., Smit, C. A., Perchuk, L. L., Kramers, J. D. & Armstrong, R. (2006). Geologic history of the Central Zone of the Limpopo Complex: the West Alldays area. *Journal of Geology* **114**, 699–716.

Bracciali, L., Parrish, R. R., Horstwood, M. S. A., Condon, D. J. & Najman, Y. (2013). U–Pb LA-(MC)-ICP-MS dating of rutile: new reference materials and applications to sedimentary provenance. *Chemical Geology* **347**, 82–101.

Brandt, S., Klemd, R., Li, Q., Kröner, A., Brandl, G., Fischer, A., Bobek, P. & Zhou, T. (2018). Pressure–temperature evolution during two granulite-facies metamorphic events (2·62 and 2·02 Ga) in rocks from the Central Zone of the Limpopo Belt, South Africa. *Precambrian Research* **310**, 471–506.

Brown, M. & Dallmeyer, R. D. (1996). Rapid Variscan exhumation and the role of magma in core complex formation: Southern Brittany metamorphic belt, France. *Journal of Metamorphic Geology* **14**, 361–379.

Brown, M. & Solar, G. S. (1998). Shear-zone systems and melts: feedback relations and self-organization in orogenic belts. *Journal of Structural Geology* **20**, 211–227.

Brown, M., Averkin, Y. A., McLellan, E. L. & Sawyer, E. W. (1995). Melt segregation in migmatites. *Journal of Geophysical Research: Solid Earth* **100**, 15655–15679.

Brun, J. P., Gapais, D. & Le Theoff, B. (1981). The mantled gneiss domes of Kuopio (Finland): interfering diapirs. *Tectonophysics* **74**, 283–304.

Carrington, D. P. & Harley, S. L. (1995). Partial melting and phase relations in high-grade metapelites: an experimental petrogenetic grid in the KFMASH system. *Contributions to Mineralogy and Petrology* **120**, 270–291.

Cesare, B., Acosta-Vigil, A., Bartoli, O. & Ferrero, S. (2015). What can we learn from melt inclusions in migmatites and granulites? *Lithos* **239**, 186–216.

Connolly, J. A. D. (2005). Computation of phase equilibria by linear programming: A tool for geodynamic modeling and its application to subduction zone decarbonation. *Earth and Planetary Science Letters* **236**, 524–541.

Dirks, P. H. G. M., Zhang, J. S. & Passchier, C. W. (1997). Exhumation of high-pressure granulites and the role of lower crustal advection in the North China craton near Datong. *Journal of Structural Geology* **19**, 1343–1358.

Droop, G. T. (1989). Reaction history of garnet–sapphirine granulites and conditions of Archaean high-pressure granulite-facies metamorphism in the Central Limpopo Mobile Belt, Zimbabwe. *Journal of Metamorphic Geology* **7**, 383–403.

Eskola, P. E. (1948). The problem of mantled gneiss domes. *Quarterly Journal of the Geological Society* **104**, 461–476.

Fripp, R. E. P. (1983) The Precambrian geology of the area around the Sand River near Messina, Central Zone, Limpopo Mobile Belt. In: van Biljon W. J. & Legg J. H. (eds) *The Limpopo Mobile Belt*, Vol. **8**. Geological Society of South Africa: Special Publications, pp.89–102.

Fuhrman, M. L. & Lindsley, D. H. (1988). Ternary-feldspar modeling and thermometry. *American Mineralogist* **73**, 201–215.

Geisler, T., Schaltegger, U. & Tomaschek, F. (2007). Re-equilibration of zircon in aqueous fluids and melts. *Elements* **3**, 43–50.

Gervais, F., Nadeau, L., Malo, M., Whitney, D. L., Teyssier, C. & Siddoway, C. S. (2004). Migmatitic structures and solid-state diapirism in orthogneiss domes, eastern Grenville Province, Canada. In: Whitney, D., Teyssier, C. & Siddoway, C. S. (eds) *Gneiss Domes in Orogeny. Geological Society of America, Special Papers* **380**, 359–378.

Haefeker, U., Kaindl, R. & Tropper, P. (2013). Improved calibrations for Raman-spectroscopic determinations of CO_2 in cordierite using three excitation wavelengths (488, 515 and 633 nm). *European Journal of Mineralogy* **25**, 745–753.

Harley, S. L., Thompson, P., Hensen, B. J. & Buick, I. S. (2002). Cordierite as a sensor of fluid conditions in high-grade metamorphism and crustal anatexis. *Journal of Metamorphic Geology* **20**, 71–86.

Harlov, D. E. & Dunkley, D. (2010). Experimental high-grade alteration of zircon using alkali and Ca-bearing solutions: resetting the zircon geochronometer during metasomatism. *American Geophysical Union, Fall Meeting, Abstract* V41D–V2301D.

Henry, D. J., Guidotti, C. V. & Thomson, J. A. (2005). The Ti-saturation surface for low-to-medium pressure metapelitic biotites: implications for geothermometry and Ti-substitution mechanisms. *American Mineralogist* **90**, 316–328.

Hiroi, Y., Motoyoshi, Y., Ellis, D. J., Shiraishi, K. & Kondo, Y. (1997) The significance of phosphorus zonation in garnet from high grade pelitic rocks: A new indicator of partial melting. In: (Ricci C. A. (ed)) *The Antarctic Region: Geological Evolution and Processes. Proceedings of the VII International Symposium on Antarctic Earth Sciences, Siena. Terra Antartica*, Vol. **73**, p.77.

Hiroi, Y., Yanagi, A., Kato, M., Kobayashi, T., Prame, B., Hokada, T., Satish-Kumar, M., Ishikawa, M., Adachi, T., Osanai, Y. & Motoyoshi, Y. (2014). Supercooled melt inclusions in lower-crustal granulites as a consequence of rapid exhumation by channel flow. *Gondwana Research* **25**, 226–234.

Hisada, K., Perchuk, L. L., Gerya, T. V., van Reenen, D. D. & Paya, B. K. (2005). *P–T*–fluid evolution in the Mahalapye Complex, Limpopo high-grade terrane, eastern Botswana. *Journal of Metamorphic Geology* **23**, 313–334.

Holdaway, M. J. (1971). Stability of andalusite and the aluminosilicate phase diagram. *American Journal of Science* **271**, 97–131.

Holland, T. J. B. & Powell, R. (2011). An improved and extended internally consistent thermodynamic dataset for phases of petrological interest, involving a new equation of state for solids. *Journal of Metamorphic Geology* **29**, 333–383.

Holzer, L., Frei, R., Barton, J. M., Jr. & Kramers, J. D. (1998). Unraveling the record of successive high grade events in the Central Zone of the Limpopo Belt using Pb single phase dating of metamorphic minerals. *Precambrian Research* **87**, 87–115.

Horrocks, P. C. (1983) The Precambrian geology of an area between Messina and Tshipise, Limpopo mobile belt. In: (Van Biljon W. J. & Legg J. H. (eds)) *The Limpopo Mobile Belt. Geological Society of South Africa, Special Publications*, Vol. **8**, pp.81–88.

Huhma, H., Mänttäri, I., Peltonen, P., Kontinen, A., Halkoaho, T., Hanski, E., Hokkanen, T., Hölttä, P., Juopperi, H., Konnunaho, J., Lahaye, Y., Luukkonen, E., Pietikäinen, K., Pulkkinen, A., Sorjonen-Ward, P., Vaasjoki, M. & Whitehouse, M. (2012). The age of the Archaean greenstone belts in Finland. *Geological Survey of Finland, Special Paper* **54**, 74–175.

Jackson, S. E., Pearson, N. J., Griffin, W. L. & Belousova, E. A. (2004). The application of laser ablation-inductively coupled plasma-mass spectrometry to *in situ* U–Pb zircon geochronology. *Chemical Geology* **211**, 47–69.

Jaeckel, P., Kröner, A., Kamo, S. L., Brandl, G. & Wendt, J. I. (1997). Late Archaean to early Proterozoic granitoid magmatism and high-grade metamorphism in the Central Limpopo belt, South Africa. *Journal of the Geological Society, London* **154**, 25–44.

Jamieson, R. A., Unsworth, M. J., Harris, N. B., Rosenberg, C. L. & Schulmann, K. (2011). Crustal melting and the flow of mountains. *Elements* **7**, 253–260.

Jarosewich, E., Nelen, J. A. & Norberg, J. A. (1980). Reference samples for electron microprobe analysis. *Geostandards Newsletter* **4**, 43–47.

Johannes, W. & Schreyer, W. (1981). Experimental introduction of CO_2 and H_2O into Mg-cordierite. *American Journal of Science* **281**, 299–317.

Kawakami, T. & Hokada, T. (2010). Linking *PT* path with development of discontinuous phosphorus zoning in garnet during high-temperature metamorphism—an example from Lützow–Holm Complex, East Antarctica. *Journal of Mineralogical and Petrological Sciences* **105**, 175–186.

Kawakami, T. & Motoyoshi, Y. (2004). Timing of attainment of the spinel + quartz coexistence in garnet–sillimanite leucogneiss from Skallevikshalsen, Lützow–Holm Complex, East Antarctica. *Journal of Mineralogical and Petrological Sciences* **99**, 311–319.

Kawasaki, T. & Motoyoshi, Y. (2007) Solubility of TiO_2 in garnet and orthopyroxene: Ti thermometer for ultrahigh-temperature granulites. In: Cooper A. K., Barrett P., Stagg H. *et al.* (eds) *Antarctica: A keystone in a changing world. US Geological Survey, Open-File Report 2007-1047. Short Research Paper*, Vol. **038**.

Kerrick, D. M. & Jacobs, G. K. (1981). A modified Redlich–Kwong equation for H_2O, CO_2, and H_2O–CO_2 mixtures at elevated pressures and temperatures. *American Journal of Science* **281**, 735–767.

Kobayashi, T., Hirajima, T., Kawakami, T. & Svojtka, M. (2011). Metamorphic history of garnet-rich gneiss at Ktiš in the Lhenice shear zone, Moldanubian Zone of the southern Bohemian Massif, inferred from inclusions and compositional zoning of garnet. *Lithos* **124**, 46–65.

Koester, E., Pawley, A. R., Fernandes, L. A., Porcher, C. C. & Soliani, E., Jr. (2002). Experimental melting of cordierite gneiss and the petrogenesis of syntranscurrent peraluminous granites in southern Brazil. *Journal of Petrology* **43**, 1595–1616.

Kolesov, B. A. & Geiger, C. A. (2000). Cordierite II: the role of CO_2 and H_2O. *American Mineralogist* **85**, 1265–1274.

Kramers, J. & Mouri, H. (2011). The geochronology of the Limpopo Complex: a controversy resolved. In: van Reenen D. D., Kramers J. D., McCourt S. *et al.* (eds) *Origin and Evolution of Precambrian High-Grade Gneiss Terranes, with Special Emphasis on the Limpopo Complex of Southern Africa. Geological Society of America, Memoirs* **207**, 85–105.

Kröner, A., Jaeckel, P., Hofmann, A., Nemchin, A. A. & Brandl, G. (1998). Field relationships and age of supracrustal Beit Bridge Complex and associated granitoid gneisses in the Central Zone of the Limpopo Belt, South Africa. *South African Journal of Geology* **101**, 201–213.

Kröner, A., Jaeckel, P., Brandl, G., Nemchin, A. A. & Pidgeon, R. T. (1999). Single zircon ages for granitoid gneisses in the Central Zone of the Limpopo Belt, Southern Africa and geodynamic significance. *Precambrian Research* **93**, 299–337.

Kröner, A., Brandl, G., Brandt, S., Klemd, R. & Xie, H. (2018). Geochronological evidence for Archaean and Palaeoproterozoic polymetamorphism in the central zone of the Limpopo Belt, South Africa. *Precambrian Research* **310**, 320–347.

Kruckenberg, S. C., Vanderhaeghe, O., Ferre, E. C., Teyssier, C. & Whitney, D. L. (2011). Flow of partially molten crust and the internal dynamics of a migmatite dome, Naxos, Greece. *Tectonics* **30**, TC3001.

Laurent, O., Martin, H., Doucelance, R., Moyen, J. F. & Paquette, J. L. (2011). Geochemistry and petrogenesis of high-K 'sanukitoids' from the Bulai pluton, Central Limpopo Belt, South Africa: implications for geodynamic changes at the Archaean–Proterozoic boundary. *Lithos* **123**, 73–91.

Laurent, O., Doucelance, R., Martin, H. & Moyen, J. F. (2013). Differentiation of the late-Archaean sanukitoid series and some implications for crustal growth: insights from geochemical modelling on the Bulai pluton, Central Limpopo Belt, South Africa. *Precambrian Research* **227**, 186–203.

Le Breton, N. & Thompson, A. B. (1988). Fluid-absent (dehydration) melting of biotite in metapelites in the early stages of crustal anatexis. *Contributions to Mineralogy and Petrology* **99**, 226–237.

Lexa, O., Schulmann, K., Janoušek, V., Štípská, P., Guy, A. & Racek, M. (2011). Heat sources and trigger mechanisms of exhumation of HP granulites in Variscan orogenic root. *Journal of Metamorphic Geology* **29**, 79–102.

Li, X., Zhang, C., Behrens, H. & Holtz, F. (2020). Calculating biotite formula from electron microprobe analysis data using a machine learning method based on principal components regression. *Lithos* **356**, 105371.

London, D., Wolf, M. B., Morgan, G. B. & Garrido, M. G. (1999). Experimental silicate–phosphate equilibria in peraluminous granitic magmas, with a case study of the Alburquerque batholith at Tres Arroyos, Badajoz, Spain. *Journal of Petrology* **40**, 215–240.

Ludwig, K. R. (2008). Manual for Isoplot 3.7: a geochronological toolkit for Microsoft Excel. *Berkeley Geochronology Center, Special Publications* **4**, 77.

Millonig, L., Zeh, A., Gerdes, A. & Klemd, R. (2008). Neoarchaean high-grade metamorphism in the Central Zone of the Limpopo Belt (South Africa): combined petrological and geochronological evidence from the Bulai pluton. *Lithos* **103**, 333–351.

Millonig, L. J., Zeh, A., Gerdes, A., Klemd, R. & Barton, J. M., Jr. (2010). Decompressional heating of the Mahalapye Complex, Limpopo Belt, Botswana: a response to Palaeoproterozoic magmatic underplating? *Journal of Petrology* **51**, 703–729.

Perchuk, A. L. & Philippot, P. (2000). Geospeedometry and time scales of high-pressure metamorphism. *International Geology Review* **42**, 207–223.

Perchuk, L. L., Gerya, T. V., van Reenen, D. D., Safonov, O. G. & Smit, C. A. (1996). The Limpopo Metamorphic Belt, South Africa: 2. Decompression and cooling regimes of granulites and adjacent rocks of the Kaapvaal Craton. *Petrology* **4**, 571–599.

Perchuk, L. L., Gerya, T. V., van Reenen, D. D., Smit, C. A., Krotov, A. V. & Safonov, O. G. (2000). Comparative petrology and metamorphic evolution of the Limpopo (South Africa) and Lapland (Fennoscandia) high grade terranes. *Mineralogy and Petrology* **69**, 69–107.

Perchuk, L. L., van Reenen, D. D., Smit, C. A., Boshoff, R., Belyanin, G. A. & Yapaskurt, V. O. (2008a). Role of granite intrusions for the formation of ring structures in granulite complexes: examples from the Limpopo belt, South Africa. *Petrology* **16**, 652–678.

Perchuk, L. L., van Reenen, D. D., Varlamov, D. A., van Kal, S. M. & Boshoff, R. (2008b). *P–T* record of two high-grade metamorphic events in the Central Zone of the Limpopo Complex, South Africa. *Lithos* **103**, 70–105.

Prior, D. J. (1993). Sub-critical fracture and associated retrogression of garnet during mylonitic deformation. *Contributions to Mineralogy and Petrology* **113**, 545–556.

Rajesh, H. M., Belyanin, G. A., Safonov, O. G., Vorster, C. & van Reenen, D. D. (2018a). Garnet-bearing low-Sr and high-Sr Singelele leucogranite: a record of Neoarchean episodic melting in collisional setting and Paleoproterozoic overprint in the Beit Bridge complex, southern Africa. *Lithos* **322**, 67–86.

Rajesh, H. M., Safonov, O. G., Basupi, T. O., Belyanin, G. A. & Tsunogae, T. (2018b). Complexity of characterizing granitoids in high-grade terranes: an example from the Neoarchean Verbaard granitoid, Limpopo Complex, Southern Africa. *Lithos* **318**, 399–418.

Rajesh, H. M., Safonov, O. G., Belyanin, G. A. & Vorster, C. (2020). A ~2·051 Ga anatectic event and peraluminous leucogranite from the Mahalapye Complex, northern edge of the Kaapvaal Craton: record of an effect of Bushveld mafic magmatism. *Lithos* **378-379**, 105805.

Ramberg, H. (1981). *Gravity, Deformation and the Earth's Crust*. London: Academic Press, 452 p.

Roering, C., van Reenen, D. D., de Wit, M. J., Smit, C. A., de Beer, J. H. & van Schalkwyk, J. F. (1992). Structural geological and metamorphic significance of the Kaapvaal craton–Limpopo Belt contact. *Precambrian Research* **55**, 69–80.

Rosa, D. R. N., Finch, A. A., Andersen, T. & Inverno, C. M. C. (2009). U–Pb geochronology and Hf isotope ratios of magmatic zircons from the Iberian Pyrite Belt. *Mineralogy and Petrology* **95**, 47–69.

Rosenberg, C. L. & Handy, M. R. (2005). Experimental deformation of partially melted granite revisited: implications for the continental crust. *Journal of Metamorphic Geology* **23**, 19–28.

Schäller, M., Steiner, O., Studer, I., Holzer, L., Herwegh, M. & Kramers, J. D. (1999). Exhumation of Limpopo Central Zone granulites and dextral continent-scale transcurrent movement at 2·0 Ga along the Palala shear zone, Northern Province, South Africa. *Precambrian Research* **96**, 263–288.

Schoene, B., Crowley, J. L., Condon, D. J., Schmitz, M. D. & Bowring, S. A. (2006). Reassessing the uranium decay constants for geochronology using ID-TIMS U–Pb data. *Geochimica et Cosmochimica Acta* **70**, 426–445.

Smit, C. A., van Reenen, D. D., Roering, C., Boshoff, R. & Perchuk, L. L. (2011). Neoarchean to Paleoproterozoic evolution of the polymetamorphic Central Zone of the Limpopo Complex. In: van Reenen D. D., Kramers J. D., McCourt S. *et al.* (eds) *Origin and Evolution of Precambrian High-Grade Gneiss Terranes, with Special Emphasis on the Limpopo Complex of Southern Africa. Geological Society of America, Memoirs* **207**, 213–244.

Stacey, J. S. & Kramers, J. D. (1975). Approximation of terrestrial lead isotope evolution by a two-stage model. *Earth and Planetary Science Letters* **26**, 207–221.

Stern, R. A., Bodorkos, S., Kamo, S., Hickman, A. H. & Corfu, F. (2009). Measurement of SIMS instrumental mass fractionation of Pb isotopes during zircon dating. *Geostandards and Geoanalytical Research* **33**, 145–168.

Stevens, G., Clemens, J. D. & Droop, G. T. (1995). Hydrous cordierite in granulites and crustal magma production. *Geology* **23**, 925–928.

Teyssier, C. & Whitney, D. L. (2002). Gneiss domes and orogeny. *Geology* **30**, 1139–1142.

Tsunogae, T. & van Reenen, D. D. (2006). Corundum + quartz and Mg-staurolite bearing granulite from the Limpopo Belt, southern Africa: implications for a *P–T* path. *Lithos* **92**, 576–587.

Tsunogae, T. & van Reenen, D. D. (2011). High-pressure and ultrahigh-temperature granulite-facies metamorphism of Precambrian high-grade terranes: case study of the Limpopo Complex. In: van Reenen D. D., Kramers J. D., McCourt S. *et al.* (eds) *Origin and Evolution of Precambrian High-Grade Gneiss Terranes, with Special Emphasis on the Limpopo Complex of Southern Africa. Geological Society of America, Memoirs* **207**, 107–124.

Vanderhaeghe, O. (2009). Migmatites, granites and orogeny: flow modes of partially-molten rocks and magmas associated with melt/solid segregation in orogenic belts. *Tectonophysics* **477**, 119–134.

Vanderhaeghe, O. & Teyssier, C. (2001). Partial melting and flow of orogens. *Tectonophysics* **342**, 451–472.

van Kal, S. (2004) *Two distinct tectono-metamorphic events in the Central Zone of the Limpopo Complex, South Africa: evidence from the Mt Shanzi sheath fold and the Campbell cross fold near Musina*. MSc thesis. Rand Afrikaans University, Jhannesburg, South Africa.

van Reenen, D. D., Boshoff, R., Smit, C. A., Perchuk, L. L., Kramers, J. D., McCourt, S. & Armstrong, R. A. (2008). Geochronological problems related to polymetamorphism in the Limpopo Complex, South Africa. *Gondwana Research* **14**, 644–662.

van Reenen, D. D., Smit, C. A., Perchuk, A. L., Huizenga, J.-M., Safonov, O. G. & Gerya, T. V. (2019) The Neoarchaean Limpopo Orogeny: Exhumation and regional-scale gravitational crustal overturn driven by a granulite diapir. In: Kröner A. & Hofmann A. (eds) *The Archaean Geology of the Kaapvaal Craton*. Southern Africa. Cham: Springer, pp.185–224.

Vielzeuf, D. & Holloway, J. R. (1988). Experimental determination of the fluid-absent melting relations in the pelitic system: consequences for crustal differentiation. *Contributions to Mineralogy and Petrology* **98**, 257–276.

Watkeys, M. K. (1979). Explanation of the geological map of the country west of Beit Bridge. *Short Report of the Geological Survey of Rhodesia* **45**, 96.

Weinberg, R. F. (1997). Diapir-driven crustal convection: decompression melting, renewal of the magma source and the origin of nested plutons. *Tectonophysics* **271**, 217–229.

Weinberg, R. F. & Hasalová, P. (2015). Water-fluxed melting of the continental crust: a review. *Lithos* **212**, 158–188.

Weinberg, R. F. & Podladchikov, Y. Y. (1995). The rise of solid-state diapirs. *Journal of Structural Geology* **17**, 1183–1195.

White, R. W., Powell, R., Holland, T. J. & Worley, B. A. (2000). The effect of TiO_2 and Fe_2O_3 on metapelitic assemblages at greenschist and amphibolite facies conditions: mineral equilibria calculations in the system K_2O–FeO–MgO–Al_2O_3–SiO_2–H_2O–TiO_2–Fe_2O_3. *Journal of Metamorphic Geology* **18**, 497–511.

White, R. W., Powell, R., Holland, T. J. B., Johnson, T. E. & Green, E. C. R. (2014). New mineral activity–composition relations for thermodynamic calculations in metapelitic systems. *Journal of Metamorphic Geology* **32**, 261–286.

Whitney, D. L. (1996). Garnets as open systems during regional metamorphism. *Geology* **24**, 147–150.

Whitney, D. L. & Evans, B. W. (2010). Abbreviations for names of rock-forming minerals. *American Mineralogist* **95**, 185–187.

Whitney, D. L., Teyssier, C. & Vanderhaeghe, O. (2004). Gneiss domes and crustal flow. In: Whitney, D. L., Teyssier, C. & Siddoway, C. S. (eds) *Gneiss Domes in Orogeny, Geological Society of America, Special Papers* **380**, 15–33.

Wiest, J. D., Fossen, H. & Jacobs, J. (2020). Shear zone evolution during core complex exhumation—implications for continental detachments. *Journal of Structural Geology* **140**, 104139.

Yakymchuk, C. (2017). Behaviour of apatite during partial melting of metapelites and consequences for prograde suprasolidus monazite growth. *Lithos* **274**, 412–426.

Yakymchuk, C. & Acosta-Vigil, A. (2019). Geochemistry of phosphorus and the behavior of apatite during crustal anatexis: insights from melt inclusions and nanogranitoids. *American Mineralogist* **104**, 1765–1780.

Yang, P. & Rivers, T. (2002). The origin of Mn and Y annuli in garnet and the thermal dependence of P in garnet and Y in apatite in calc-pelite and pelite, Gagnon terrane, western Labrador. *Geological Materials Research* **4**, 1–35.

Yin, A. (2004). Gneiss domes and gneiss dome systems. In: Whitney, D. L., Teyssier, C. & Siddoway, C. S. (eds) *Gneiss Domes in Orogeny. Geological Society of America, Special Papers* **380**, 1–14.

Zeh, A., Klemd, R., Buhlmann, S. & Barton, J. M. (2004). Pro-and retrograde *P–T* evolution of granulites of the Beit Bridge complex (Limpopo Belt, South Africa): constraints from quantitative phase diagrams and geotectonic implications. *Journal of Metamorphic Geology* **22**, 79–95.

Zeh, A., Gerdes, A., Klemd, R. & Barton, J. M., Jr. (2007). Archaean to Proterozoic crustal evolution in the central zone of the Limpopo Belt (South Africa–Botswana): constraints from combined U–Pb and Lu–Hf isotope analyses of zircon. *Journal of Petrology* **48**, 1605–1639.